Title
LOW-ENERGY NEGATIVE PION INTERACTIONS IN DEUTERIUM

Author
Bowman, William C.

Publication Date
1963-09-05

UCRL-10977

University of California

Ernest O. Lawrence Radiation Laboratory

LOW-ENERGY NEGATIVE PION INTERACTIONS IN DEUTERIUM

DISCLAIMER

Research and Development

UCRL-10977
UC-34 Physics
TID-4500 (19th Ed)

UNIVERSITY OF CALIFORNIA

Lawrence Radiation Laboratory
Berkeley, California

AEC Contract No. W-7405-eng-48

LOW-ENERGY NEGATIVE PION INTERACTIONS IN DEUTERIUM

William C. Bowman

(Ph. D. Thesis)

September 5, 1963

Printed in USA. Price $2.00. Available from the
Office of Technical Services
U. S. Department of Commerce
Washington 25, D.C.

LOW-ENERGY NEGATIVE PION INTERACTIONS IN DEUTERIUM

Contents

LOW-ENERGY NEGATIVE PION INTERACTIONS IN DEUTERIUM

William C. Bowman

Lawrence Radiation Laboratory
University of California
Berkeley, California

September 5, 1963

ABSTRACT

This work is an attempt to resolve the discrepancy between the measured deuterium ratio, $S = \frac{\omega(\pi^- + d \rightarrow n + n)}{\omega(\pi^- + d \rightarrow n + n + \gamma)}$, and values predicted from the s-wave pion relations and the theoretically calculated ratio $T = \frac{\omega(\pi^- + d \rightarrow n + n + \gamma)}{\omega(\pi^- + p \rightarrow n + \gamma)}$.

The cross sections $\sigma(\pi^- + d \rightarrow n + n + \gamma) = (3.78 \pm 0.79) \times 10^{-20}$ cm^2/steradian, $\sigma(\pi^- + d \rightarrow n + n) = (3.67 \pm 0.45) \times 10^{-28}$ cm^2/sr, and $\sigma(\pi^- + d \rightarrow \pi^0 + n + n) = (7.84 \pm 0.57) \times 10^{-28}$ cm^2/sr were measured at 90 deg in the center-of-mass system for 51-MeV incident pion energy. The radiative absorption cross section and the s-wave pion relations indicate the value of $T = 0.91 \pm 0.19$, in agreement with theoretical calculations. The calculation of $S = 1.51 \pm 0.40$ from the cross section measurements and the value $S = 1.92 \pm 0.33$ measured by direction detection of both reactions is in agreement with the value $S = 1.74 \pm 0.26$ calculated from the s-wave pion relations. An indirect measurement comparing radiative captures in hydrogen and deuterium gave a value of $S = 3.37 \pm 0.46$, in relative agreement with other indirect measurements. This discrepancy appears to be due to difficulty in monitoring the number of pions captured in hydrogen and deuterium.

A total-absorption plastic scintillation counter was used for all measurements.

I. INTRODUCTION

When negative pions are incident on deuterium the following interactions are possible:

$$\pi^- + d \rightarrow \pi^- + d, \qquad \text{elastic scattering,} \qquad (1)$$

$$\pi^- + d \rightarrow \pi^- + n + p, \qquad \text{inelastic scattering,} \qquad (2)$$

$$\pi^- + d \rightarrow \pi^0 + n + n, \qquad \text{charge-exchange scattering,} \qquad (3)$$

$$\pi^- + d \rightarrow n + n + \gamma, \qquad \text{radiative absorption,} \qquad (4)$$

$$\pi^- + d \rightarrow n + n, \qquad \text{nonradiative absorption.} \qquad (5)$$

The final-state particles in these interactions are all stable compared with the incident π^- with the exception of the π^0, which decays into two γ's in approximately 2×10^{-16} sec. The π^0 decay and Reaction (4) may proceed with the substitution of an electron-positron pair in place of a γ in the final state. Calculations by Joseph show that these pair-producing interactions in hydrogen occur no more than 1.7% of the time.[1] The impulse approximation would indicate this would also be true in deuterium. All pair-producing reactions are neglected in this paper.

The mechanisms by which mesons are slowed and captured by hydrogen and deuterium have been discussed by Wightman;[2] by Fields, Yodh, Derrick, and Fetkovich;[3] and by Russell and Shaw,[4] who follow an argument by Day, Snow, and Sucher.[5] They show that the slowing and capture processes occur quite rapidly compared with the decay time of the pion, and that nuclear capture takes place from excited S states of the mesic atom.

For the case of stopping π^- in deuterium the charge-exchange capture (3) is unlikely to occur. This can easily be shown because the capture takes place from an S state. The pion is pseudoscalar, and either in a $^3S_1$ state or $^3D_1$ state. Therefore the final state must have $J = 1$ and odd parity. The Pauli principle forbids the two neutrons from being in a $^3S_1$ state. The parity of the pion demands a spatial state of even parity in this interaction, which can most easily be satisfied when both the neutron-neutron and the neutron-pion systems are in P

states. This, however, would be difficult to achieve with the small amount of energy available in this reaction. The absence of the charge-exchange reaction for stopping π^- in deuterium has been experimentally verified by Panofsky, Aamodt, and Hadley,[6] and by Chinowsky and Steinberger.[7]

Anderson and Fermi[8] pointed out a chain of relations connecting the Panofsky ratio

$$P = \frac{\omega(\pi^- + p \rightarrow \pi^0 + n)}{\omega(\pi^- + p \rightarrow n + \gamma)} \tag{6}$$

with photopion production and pion-scattering phase shifts. Brueckner, Serber, and Watson[9] later extended this chain to connect the hydrogen reactions with pion production by nucleon-nucleon collisions, relating them through the deuterium ratio

$$S = \frac{\omega(\pi^- + d \rightarrow n + n)}{\omega(\pi^- + d \rightarrow n + n + \gamma)} \tag{7}$$

and radiative capture rates

$$T = \frac{\omega(\pi^- + d \rightarrow n + n + \gamma)}{\omega(\pi^- + p \rightarrow n + \gamma)} \quad . \tag{8}$$

This chain of relations appears in Table I.

Discrepancies between the measured Panofsky ratio and that calculated through the chain of relations have stimulated a great deal of experimental and theoretical work. The discrepancies seem to have been resolved through the theoretical work of Baldin,[10] Cini, Gatto, Goldwasser, and Ruderman,[11] and Hamilton and Woolcock,[12] and through the relative consistency of the more recent Panofsky ratio measurements as illustrated by Table II.

Table I. s-Wave pion relations.

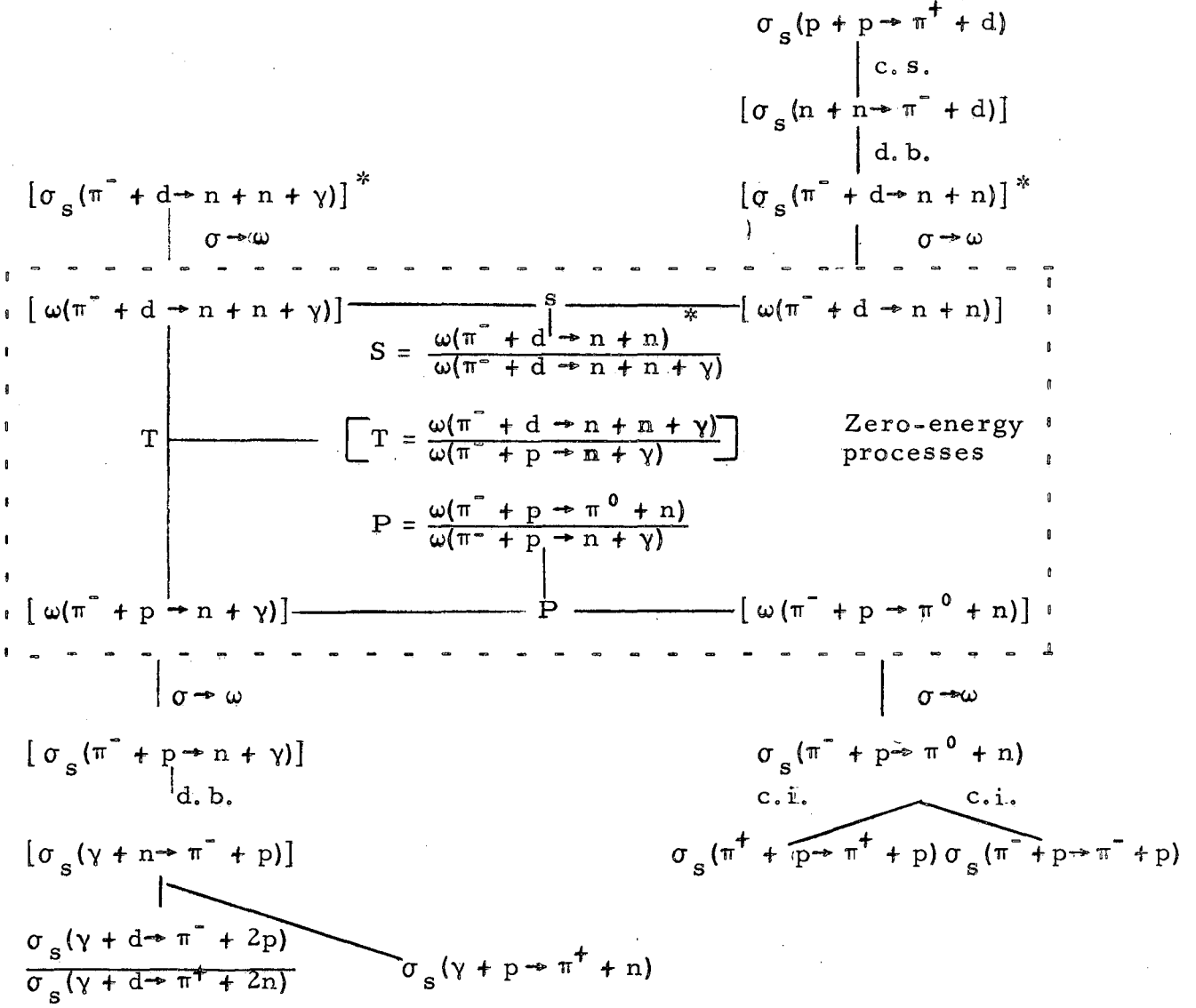

*Indicates processes measured by this experiment

[ ] indicates calculated processes

c. s. = charge symmetry

c. i. = charge independence

d. b. = detail balance

$\sigma \to \omega$ = extrapolation from cross section to transition rate.

(see Appendix A for detailed explanation)

Table II. Panofsky ratio measurements.

Experimenter	Reference	Method	P
Panofsky et al.	6	Pair spectrometer	0.94±0.30
Sargent et al.	13	Cloud chamber	1.10±0.50
Cassels et al.	14	Total-absorption Cerenkov counter	1.50±0.15
Fischer et al.	15	Total-absorption Cerenkov detector	1.87±0.10
Kuehner et al.	16	Pair spectrometer	1.60±0.17
Koller et al.	17	Total-absorption Cerenkov detector	1.46±0.10
Dunaitsev et al.	18	γ-γ coincidence	1.40±0.08
Derrick et al.	19	Bubble chamber	1.47±0.10
Samios	20	Bubble chamber	1.62±0.06
Jones et al.	21	Total-absorption Cerenkov detector	1.56±0.05
Cocconi et al.	22	Total absorption NaI detector	1.533±0.021
Ryan	23	Pair spectrometer	1.51±0.04
Weighted average			1.534±0.018

The success of the hydrogen chain of relations does not seem to be shared by the deuterium relations; this is evidenced by the discrepancy between the values of the radiative capture ratio, T, calculated through the chain of relations and the theoretical value calculated by Traxler,[24] as shown in Table III.

The radiative capture ratio, T, is a purely theoretical quantity, not subject to direct measurement. Therefore it can be verified only through such a chain of relations.

Because of the variety of experimentally measured values of the deuterium ratio, as shown in Table IV, and the aforementioned discrepancy in the calculations of the radiative capture ratio, T, we felt further work on the deuterium chain of relations was warranted. We propose to check the chain by measuring the cross sections for Reactions (4) and (5) at 50 MeV pion energy (lab) as well as remeasuring the deuterium ratio itself.

The measurement of the cross sections for Reactions (4) and (5) will permit an independent calculation of the transition rates appearing in the deuterium and radiative-capture ratios. This will supply a check on the radiative-capture ratio independent of the chain of relations in deuterium.

The measurement of the cross section for Reaction (3) gives evidence on the validity of the impulse approximation by comparison with the charge-exchange cross section in hydrogen.

The cross sections for Reactions (3), (4), and (5), when compared with those for similar reactions of π^+ in deuterium, will give a measure of the Coulomb correction, which has been neglected in the charge-symmetry assumption in the deuterium chain of relations.

Table III. Radiative capture ratio.

Author	Reference	Method	T
Traxler	24	Theoretical calculation	0.83±0.08
Panofsky et al.	6	s-wave pion relations and measured value (P = 0.094±0.30) of S*	0.61±0.20
		(P = 1.534±0.018)	0.43±0.10
Chinowsky and Steinberger	25	s-wave pion relations and measured value of S*	0.96±0.52
Kuehner et al.	26	s-wave pion relations and measured values of S*	0.61±0.12
Ryan	23	s-wave pion relations and measured value of S*	0.46±0.05
This experiment		(a) s-wave pion relations and indirectly measured value of S*	0.43±0.08
		(b) s-wave pion relations and measured value of S by direct detection*	0.75±0.85
		(c) s-wave pion relations and measured cross section $\sigma(\pi^- + d \rightarrow n + n)$**	0.91±0.19
			0.76±0.016

*$T = \frac{1}{S} \frac{\omega(\pi^- + d \rightarrow n + n)}{\omega(\pi^- + p \rightarrow n + \gamma)}$. The capture rates are calculated from the s-wave pion relations as illustrated in Appendix A.

**$T = \frac{\omega(\pi^- + d \rightarrow n + n + \gamma)}{\omega(\pi^- + p \rightarrow n + \gamma)}$. The hydrogen capture rate is calculated from the s-wave pion relations as illustrated in Appendix A. The deuterium capture rate is calculated from the measured cross section $\sigma(\pi^- + d \rightarrow n + n + \gamma)$ in a manner similar to that shown in Appendix A.

Table IV. Deuterium-ratio measurements.

Experimenter	Reference	Method	S
Panofsky et al.	6	(a) Pair spectrometer (P = 0.94±0.30)	2.36±0.74
		(b) Pair spectrometer (P = 1.534±0.018)	3.33±0.68
Chinowsky and Steinberger	25	Counter detection of both reactions	1.5±0.8
Kuehner et al.	26	Pair spectrometer (P = 1.50±0.15)	2.36±0.36
Ryan	23	Pair spectrometer (P = 1.53±0.02)	3.16±0.10
This experiment		(a) Total absorption scintillation counter (P = 1.534±0.018)	3.37±0.46
		(b) Direct detection	1.92±0.33
		(c) Measured cross sections	1.51±0.40
Calculated value from s-wave pion relations (T = 0.83±0.08)			1.74±0.26

II. EXPERIMENT

A. Experimental Method

We set about to measure the cross sections for Reactions (3), (4), and (5), and the deuterium ratio, S. To measure these cross sections one must be able to separate Reactions (3), (4), and (5) from one another as well as from Reactions (1) and (2).

Examination of these reactions shows that Reactions (1) and (2) have charged-particle final states, whereas Reactions (3), (4), and (5) have neutral final states.

Reaction (5) produces two monoenergetic neutrons with a velocity of 0.36 of the velocity of light, c, or greater, depending on the energy of the incident π^-.

Reaction (4), having a three-body final state, would appear to have a broad distribution on the energy of its photon. This is not the case, however, for stopping π^-. Previous measurements of the photon energy spectrum for stopping π^- show a marked peaking of the photon energy distribution about the maximum energy[6,23] (Fig. 1), indicating a strong neutron-neutron coupling in the final state. The impulse approximation would predict that this peaking should persist at higher energies as well. If the photon energy is well defined, the accompanying neutrons' velocity never exceeds 0.15 c at incident pion energies up to 50 MeV.

Reaction (3) has been found not to occur for the case of stopping π^-.[6,7] However, it may be expected to take place at higher energies. The π^0 thus produced quickly decays into two photons of equal energy and isotropic angular distribution in the rest frame of the π^0. The photon energy spectrum in the lab frame is spread by the velocity distribution of the π^0. The maximum photon energy from the π^0 decay is less than the maximum photon energy of Reaction (4) for the same incident pion energy. Therefore photon energy is a means of distinguishing between Reactions (3) and (4). The maximum velocity of the accompanying neutrons in Reaction (3) is 0.28 c for incident pion energies up to 50 MeV.

The experiment was carried out with a charged-particle "anti counter" surrounding the target to discriminate against Reactions (1) and (2) (i.e., to inactivate the system when a charged particle comes

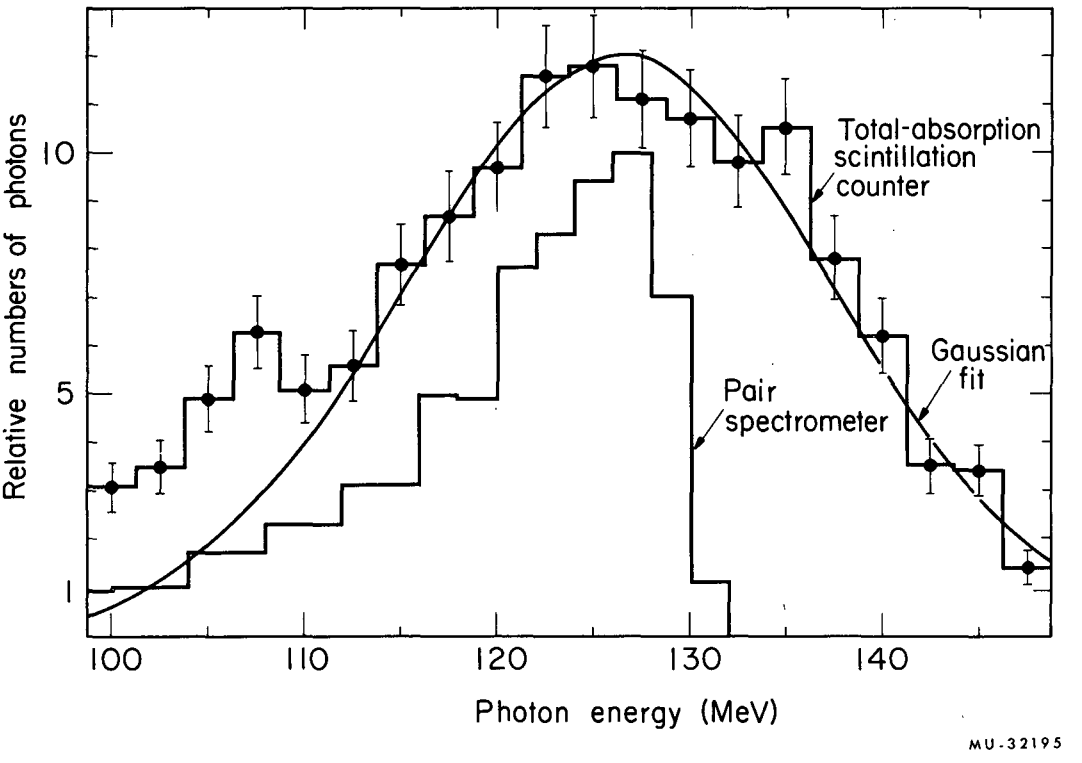

Fig. 1. A plot of the energy distribution of the capture photon in deuterium measured by a pair spectrometer (Ryan, reference 23), and by our total-absorption counter. This illustrates the comparison of our energy resolution with the actual spread in photon energy and indicates the error in assuming the photon distribution to be Gaussian (curve drawn through data).

through). The cross sections for Reactions (3) and (4) were determined by measuring the photon energy spectrum radiating from the target.

We chose to detect and measure the photon energy spectrum with a total-absorption scintillation counter.[27] This device is sensitive to neutrons as well as photons. However, since the time of flight for the neutrons from the target to the total absorption counter is different from that for photons, a separation of their pulse-height spectra is possible.

The velocities of the neutrons in Reactions (3), (4), and (5) are such as to enable us to detect the neutrons in Reaction (5) by using the total-absorption scintillation counter while excluding the neutrons from Reactions (3) and (4), thanks to the resolving time of the electronics.

The deuterium ratio, S, was determined by measuring the ratio of the number of radiative capture photons produced in hydrogen, $\#\gamma_H$, to the number of radiative capture photons produced in deuterium, $\#\gamma_D$, for a given number of stopping π^-. This ratio, when combined with the Panofsky ratio, Table II, determines S:

$$S = (P + 1)\left(\#\gamma_H/\#\gamma_D\right) - 1 . \qquad (9)$$

(This relation is derived in Section II. C. 1. a.)
The deuterium ratio was also measured directly by detecting the non-radiative capture neutrons as well as the radiative capture photon with the total-absorption scintillation counter.

The data were recorded by two separate methods. When the counter-electronics system determined that a beam particle entered the target and no charged particle emerged, yet a pulse occurred in the total absorption counter, a pulse-height analyzer was gated on to record the pulse height in the total absorption counter. Simultaneously a photograph was taken of a display of pulses on a four-beam oscilloscope from the entire counter system. Analysis of the photographs yielded correlated timing information as well as pulse-height information.

1. Beam

a. Design

The source of pions for this experiment was the Berkeley

184-inch synchrocyclotron. The pions were produced by a 725-MeV beam of protons striking a beryllium target. Pions that left the cyclotron through the meson port were focused by a quadrupole focusing magnet on the first counter, F_1, which was just outside the meson wheel, as shown in Fig. 2. The beam was then momentum-analyzed by a bending magnet and focused onto the target by another quadrupole focusing magnet.

The beam was kept short in length to minimize the loss of negative pions through their decay into a μ^- meson and an antineutrino. An effort was made in the beam design to maximize the phase space of the beam, thereby assuring the largest number of useful pions. The limits to the phase space were the size of the beam-defining counter and the aperture of the second quadrupole focusing magnet. The beam design was carried out by use of the programs OPTIK[28] and CYCLOTRON ORBITS.[29]

b. Parameters

The beam was set up from program calculations and checked by using wire-orbit techniques. The beam energy and momentum spread were measured by means of a differential range curve, Fig. 3. The procedure was to plot the number of π^- stopped in the target as a function of thickness of polyethylene degrader placed in the beam. The range of the beam particles is related to their energy. Since stopping π^- produce neutral final states, the ratio of beam monitor counts with the charged-particle "anti counter" surrounding the target in anticoincidence, to the beam monitor counts alone represents the number of stopping π^-. The beam energy incident on the target was thus measured and found to be 51±5 MeV.

Not every particle in the beam was a pion. The bending magnet selected the charge and momentum of the beam particles, so that a measurement of the particle velocities sufficed to determine the kinds of particles and their relative abundance. This measurement was carried out by a time-of-flight technique. The relative time of flight for beam particles between F_1 and F_2, appearing in Fig. 2, was measured by using zero-crossing pulse-shaping techniques and a fast tunnel diode coincidence circuitry.[30] The measurements were made periodically during

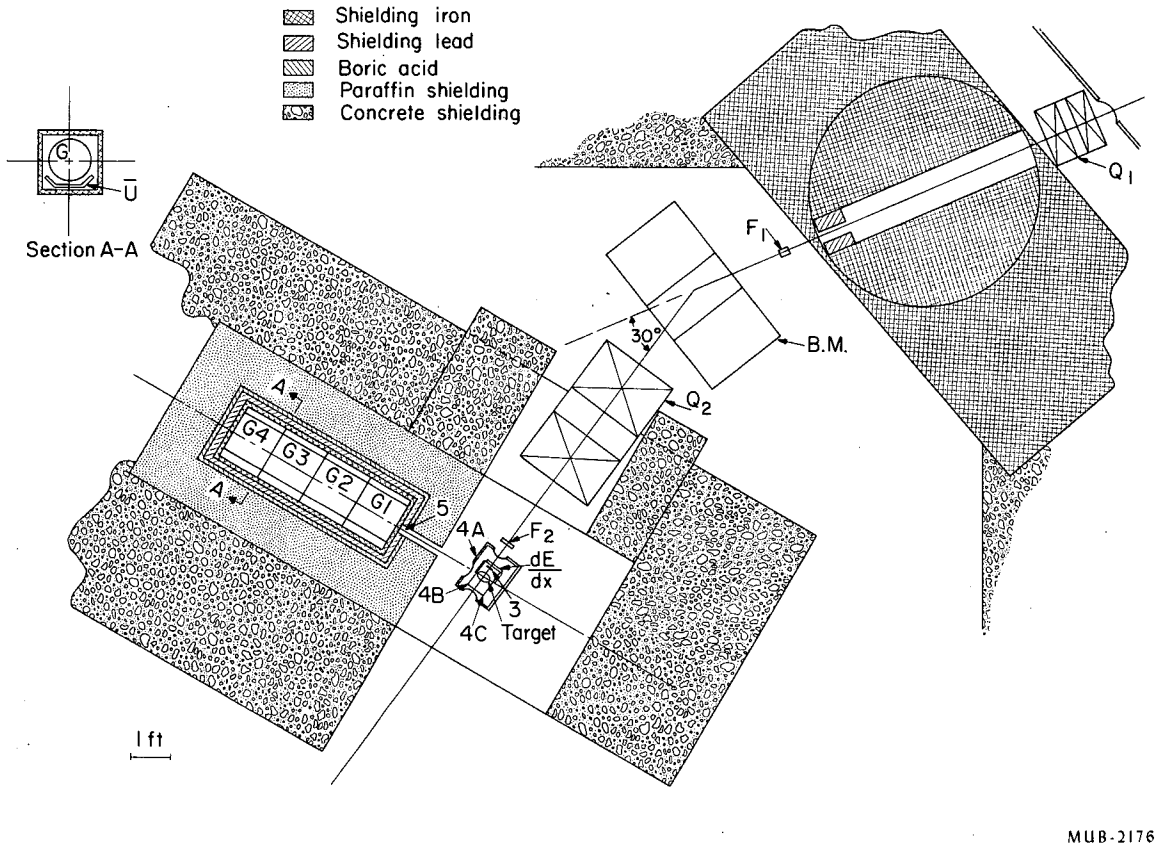

Fig. 2. A diagram of the experimental arrangement in the meson cave showing the beam layout and counter arrangement with shielding. Q_1 and Q_2 are 8-in. doublet quadrupole focusing magnets. B. M. is a bending magnet. The G's are the sections of the total-absorption counter and the $\overline{U}$ their associated cosmic ray umbrella anti counters. Only scintillator portions of the counters are shown.

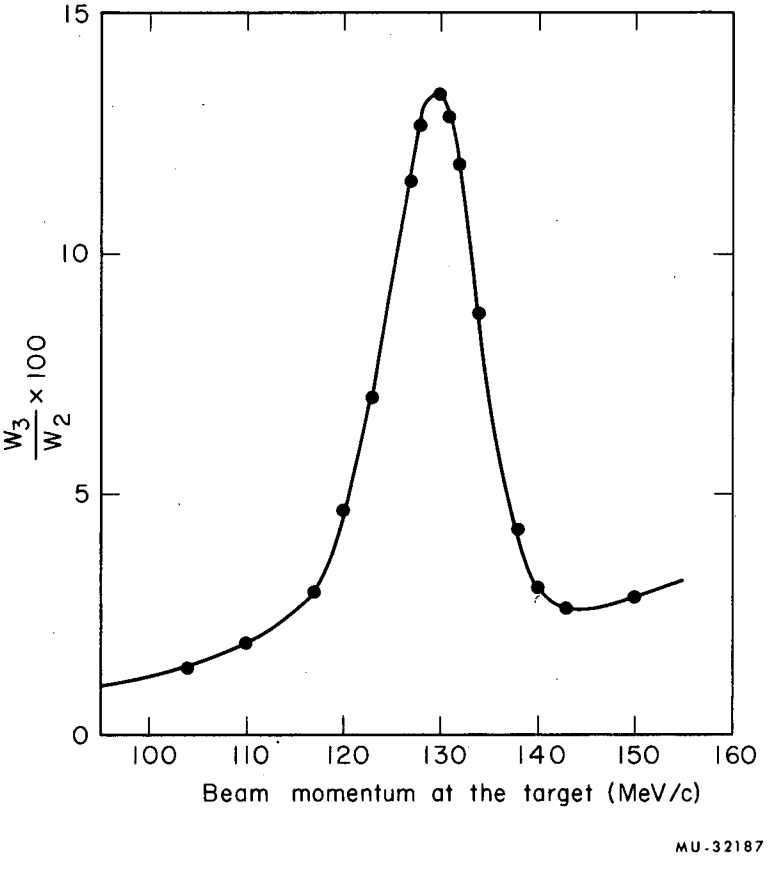

Fig. 3. A differential range curve taken in a hydrogen target and using the beam monitoring telescope with charged particle antis. The rising background is due to the increase in percentage of incident particles the scattered beam particles represents and the inefficiency of the anti for detecting them.

the experiment under the standard conditions for monitoring the beam. A typical time-of-flight distribution is shown in Fig. 4. For the purpose of separating the various components of the beam their time-of-flight distributions were assumed to be Gaussian. A Gaussian was fitted to the time distribution for each type of particle in the beam by use of a least-squares technique. On the average 70.2±1.4% of the beam was found to be pions. The remaining 29.8% was made up of muons and electrons.

The beam intensity varied between 1.5 and 2.0 million beam particles per minute.

The beam profile was measured by replacing the target with a 3/8-in.-diameter scintillation counter. The counter was moved systematically across the face of the target. The relative intensity thus measured in coincidence with the beam appears in Fig. 5. The beam profile indicates only 83.7±0.8% of the beam was incident on the target.

2. Target

a. Design

The target consisted of liquid deuterium contained in a Mylar flask. The flask was suspended in a vacuum on its Mylar fill and vent lines. The flask wall consisted of two layers of 0.0075-in. molded Mylar film. The diameter of the flask was 5 in., determined by the expected beam profile. The flask was approximately 3 in. thick. The flask thickness was determined by considering its effect on the counting rate for measured events and the probability for pion straggling. If a pion stops in deuterium, it always interacts by either Reaction (4) or (5). Thus a stopped pion would lead to an error in cross-section measurements.

Since it was desirable to surround the target with counters, it was not possible to use a standard heat shield. Therefore the flask fill and vent lines were wrapped with seven layers of 0.00025-in. doubly aluminized Mylar film to prevent boiling in the target. To further insulate the target the flask and counter system was placed in a vacuum. The vacuum can consisted of a 0.5-in.-thick aluminum box with two 8-in.-diam beam ports and a 9-in.-diam port located at 84 deg from

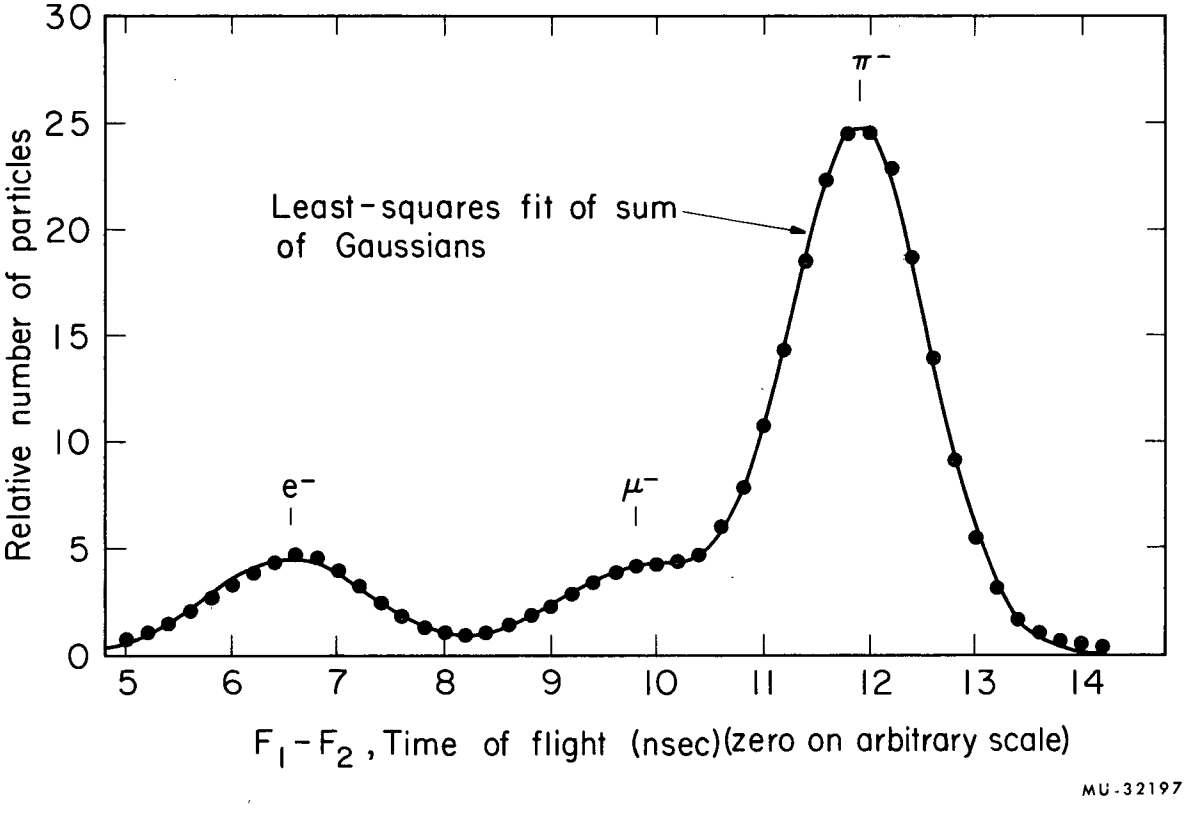

Fig. 4. A typical time-of-flight distribution for beam particles between F_1 and F_2 used to determine the beam composition. The position of the three distributions is indicated and a least-squares fit of three Gaussians drawn through the data. This fit indicates 70.6% of the beam is π^-, 13.9% of the beam is μ^-, and 15.5% of the beam is e^-.

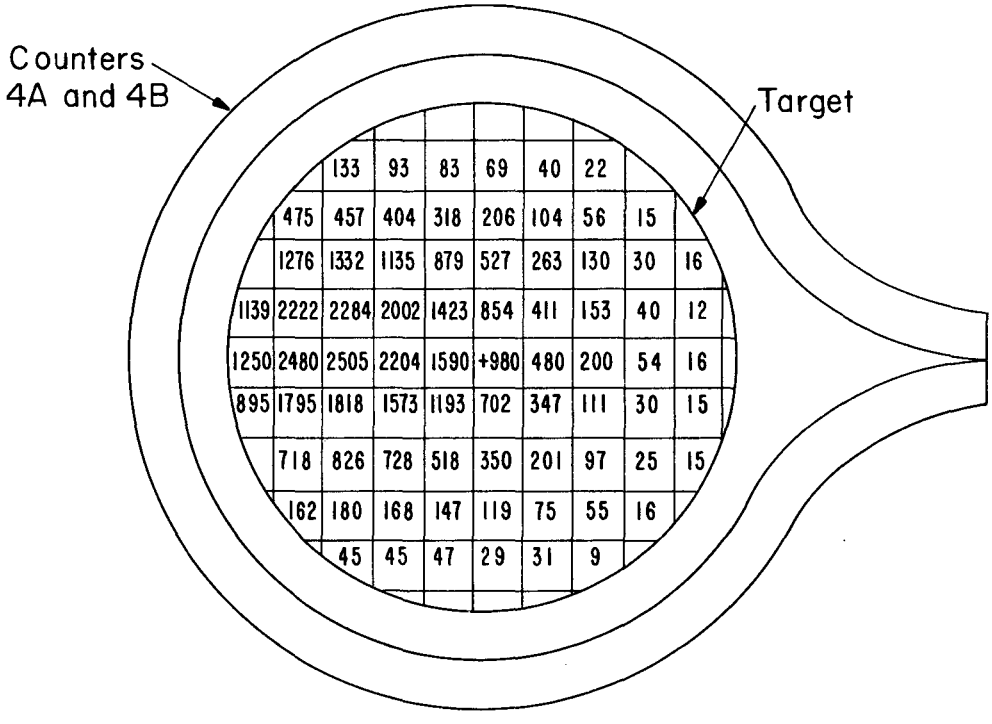

Fig. 5. The beam profile in relative numbers of incident beam particles is shown on the target looking upstream. The surrounding scintillators for anti counters #4A and #4B are also shown.

the beam line at the target center. All the ports were covered by two layers of 0.01-in.-thick Mylar film. The beam ports allowed the beam to pass through the vacuum can with a minimum of interaction. The third port afforded the total absorption counter a relatively unobstructed view of the target.

Because the counters surrounding the flask were not lighttight, the ports of the vacuum can were covered with an additional two layers of 0.001-in.-thick aluminum foil.

Figure 6 shows the target flask, surrounding counters, and vacuum can.

b. Density

The liquid deuterium was obtained by condensing deuterium gas, using liquid hydrogen as a coolant. The masses of our target gas particles were spectrographically analyzed; they were found to be pure deuterium except for a 1% contamination by HD. The liquid deuterium was kept at its own vapor pressure, which was measured and found to be 6.82±0.49 psia. This corresponds to a density of liquid deuterium of 0.16735±0.00015, according to the Cyrogenic Data Book.[31]

Since the target was obscured from view by the surrounding counters it was necessary to survey the target into position from related markings on the vacuum can. The flask relation to the vacuum can was determined by x-ray pictures of the target system. The x-ray pictures also confirmed that the flask filled properly.

The target thickness profile, Fig. 7, was obtained by removing the counter from the target, filling the target with liquid nitrogen, and surveying the flask profile, using a transit mounted on a milling head. At this time the flask was insulated in such a manner as to approximate the normal insulation and yet afford a full face view of the flask. Under these conditions it was estimated that gas from surface boiling did not constitute more than 0.1% of the volume of the flask.

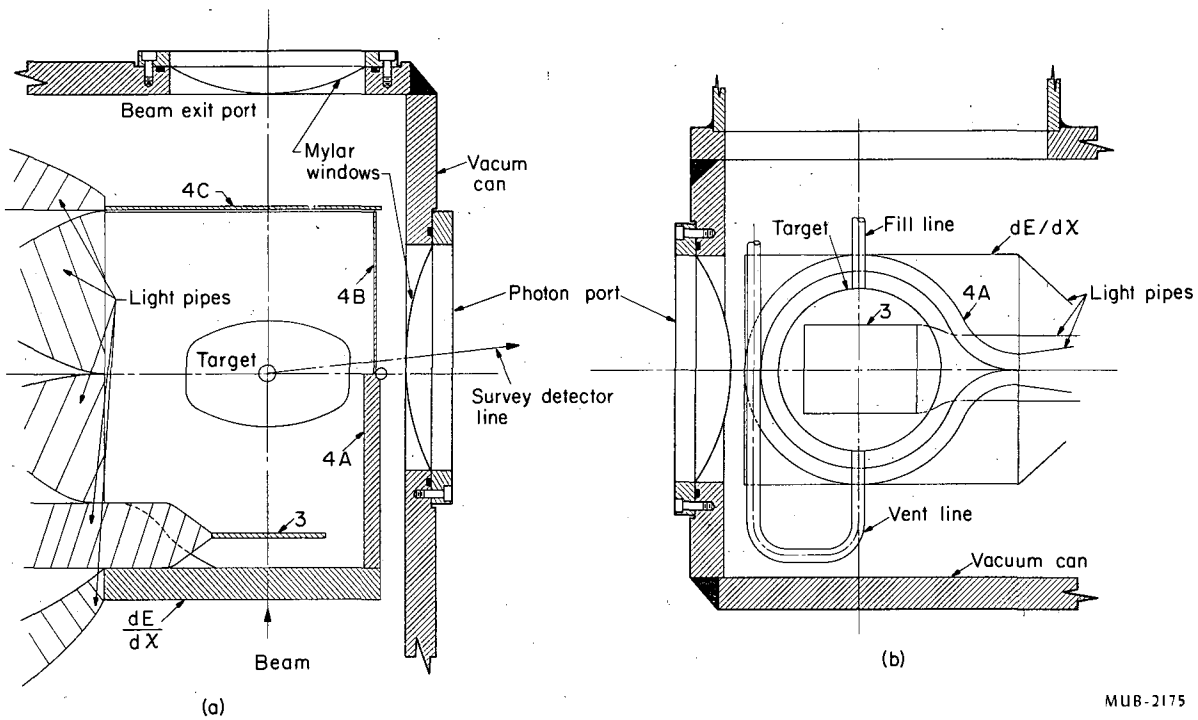

Fig. 6. Target and surrounding monitor counters ($\frac{dE}{dx}$, #3, #4, etc.). (a) Looking down on the median plane. The beam entrance port (not shown) is similar to the beam exit port. (b) Median plane, looking upstream.

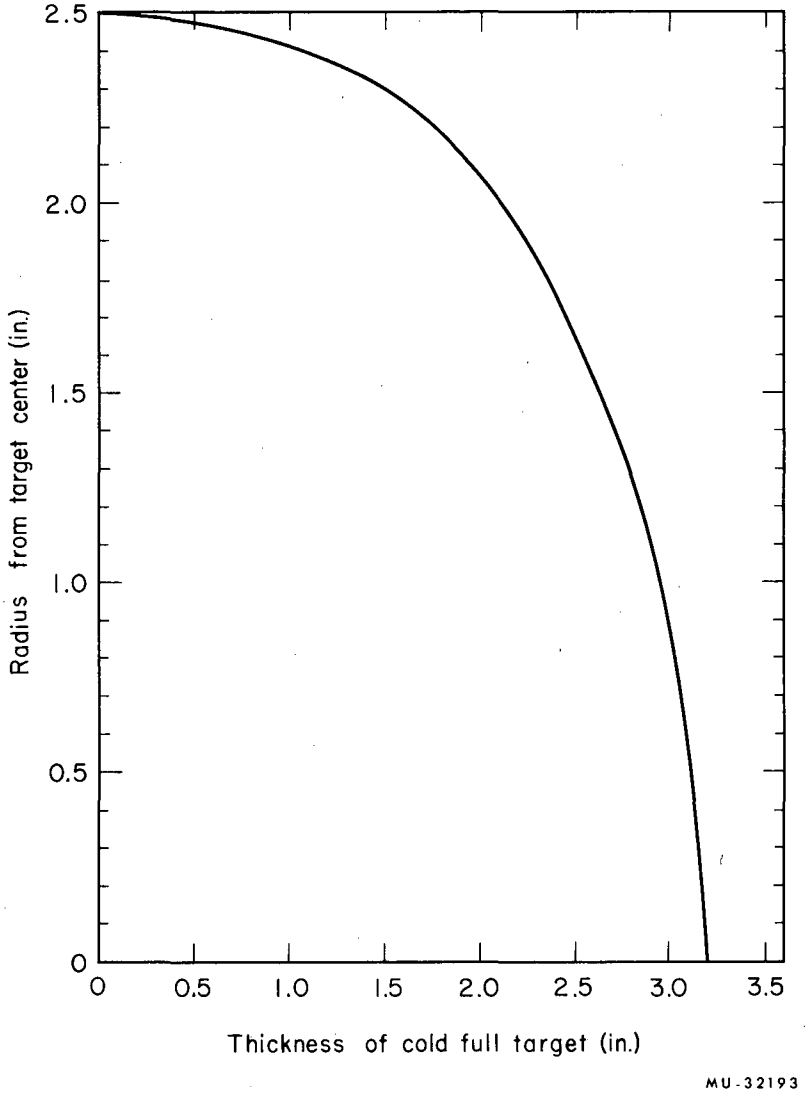

Fig. 7. A plot of the thickness of the cold full target as a function of the distance from the beam axis.

3. Counters

a. Arrangement

Figure 2 shows the arrangement of the counters. All these counters were made of plastic scintillator. Counter F_1 was 3×2×7 in. along the beam line and in the horizontal and vertical directions respectively. Counter F_2 was 1×4.5×3.75 in. These counters were designed to accommodate the beam size and give the good photoelectron statistics necessary for accurate time-of-flight work. In addition to monitoring the number of beam particles, these counters were used for time-of-flight studies of the beam composition.

The vacuum can houses a complex of counters. The first of these is a 1×8.5×7-in. dE/dx counter. The dE/dx counter was capable of resolving the energy deposited in it to within 10%. This counter was used to assure that pions in the 50-MeV beam would not stop in the target. In the energy range of the beam dE/dx is inversely proportional to the square of the particle velocity. Therefore, an upper-level discriminator was set to "anti" all pions with insufficient velocity to pass through the target. This upper-level discriminator also served to "anti" backscattered pions, since back-scattered pions would pass through the counter twice within the time width of a single pulse and produce twice the normal pulse height. The dE/dx counter was part of the beam-monitoring system.

The next counter in the vacuum can is counter #3 (0.05×3.5×2.75 in.). This was the counter that defined the beam size. This counter was kept as thin as practical so as to minimize the possible beam interactions in it. Counter #3 had an upper-level discriminator which served the same function as that used with the dE/dx counter, as well as "anti-ing" pions that interacted in the counter and produced charged-particle stars.

The last counter in the vacuum can is really three counters. Counter #4 is a charged-particle anti counter which, together with the dE/dx counter, completes a nearly 4π geometry about the target. Counter #4 has two parts, A and B, which form a near cylinder (6 in. i.d.) about the beam line, as shown in Fig. 6. The two parts of the counter

are notched to allow the flask fill and vent lines to pass between them. The downstream end of the cylinder is covered by Part C of counter #4 (0.05×8.5×7 in.). The cylinder was sufficiently long to ensure that all counters directly in the beam would be at least 5 in. from the center of the target. All the #4 counters were originally made 1/2 in. thick. Undue concern over the sensitivity of these counters to the low-energy recoil neutrons caused us to remake #4B and #4C to be 0.05 in. thick. This change in thickness reduced the efficiency of these counters to approximately 50% and 96% of the old #4B and #4C counter efficiencies, respectively.

Counter #5 is a 0.5×4×-in. counter located just behind the lead collimated aperture of the total absorption counter, and serves as a further anti for charged particles entering the total absorption counter.

Because of the physical size of the total-absorption counter there was a substantial counting rate in it due to cosmic radiation. To minimize this background an umbrella anti counter, $\overline{U}$, was placed over each section of the total absorption counter. This 0.5-in.-thick counter, approximately 2 ft wide and 80 in. long in its entirety, reduced the number of cosmic ray counts by 60%.

4. Total-Absorption Scintillation Counter

a. Design

A total-absorption plastic scintillation counter[27] was used to measure the photon spectra from Reactions (3) and (4) and to detect the neutrons from Reaction (5). The goal in the design of the total-absorption counter was to obtain a high-efficiency device with good energy resolution for photons in the energy range 10 to 200 MeV. This requirement would be satisfied by a detector whose volume was sufficient to contain all the energy of the photoelectron shower that results when a high-energy photon interacts in it. According to the data of Kantz and Hofstadter,[32] a cylinder of plastic scintillator 80 in. long and 16 in. in diameter will contain 94% of the energy of a 185-MeV electron. Since a photon interacting in the counter will produce an electron and positron each with less energy than the photon, this volume of scintillator seemed sufficient for our needs.

Because of the large variations in the solid angle subtended by a light-sensing device looking directly into so large a volume of scintillator, direct methods of detecting the scintillation light in this counter are strongly position-sensitive. In order to minimize any position sensitivity, we chose to use a light sampling technique to measure the light generated in the scintillator and thus the energy of the incident photon.

The scintillator was divided into four sections, 20 in. long, painted with a diffusely reflecting coating of α-alumina suspended in an acryloid resin in a manner similar to that of Schnurmacher.[33] Photomultiplier tubes were attached to each section to convert the scintillation light to electrical pulses. Six 2-in. photomultiplier tubes (6655A) were attached to each section; 3 in. in from each end of the section three tubes were placed in a circle around the section. Each ring was out of phase with its counterpart.

Evidence that multiple diffuse reflections occur is given by the long 20-nsec rise time of the pulse from the counter.

b. Efficiency and resolution

As the counter has been divided into four sections, it is important to ensure that 1 MeV of energy deposited in any section appears the same as in any other. To this end the high voltage on each of the photomultiplier tubes was set by using minimum-ionizing cosmic rays directed along the axis of each section. A secondary standard, a dc light source (1B59), was calibrated on the cosmic rays and used thereafter to set the high voltage of each phototube.

The energy resolution had been previously measured by observing the 129.4-MeV monoenergetic photon produced by the radiative capture of stopping pions in hydrogen in the reaction

$$\pi^- + p \rightarrow n + \gamma . \qquad (10)$$

The resolution of the measured distribution was found to be ±7% half-width at half maximum.

The efficiency of the total absorption counter for detecting photons was calculated to be 97.45±0.26%, with the length of the counter, the

radiation length in scintillator, and the fact that at least 7.5±2.5 MeV of energy has to be deposited in the counter to be detected taken into consideration.

The efficiency of the total absorption counter for detecting 70-MeV and 90-MeV neutrons has been calculated to be 41.6±4.2% and 41.1±4.1%, respectively, by use of a program developed by Richard Kurz.[34] The calculation considers a neutron incident along the axis. It considers the geometry of the counter; the counter detection threshold; the light-producing reactions C(n, α)Be, C(n, n'3α), C(n, p)B, and p(n, n)p; and the possibility of a scattered neutron's again taking part in one of these reactions.

c. Background

As has been pointed out above, the total-absorption scintillation counter is sensitive to neutrons as well as photons and charged particles. The 184-inch synchrocyclotron is a prolific source of neutrons and therefore a potential source of background. To minimize this machine background a 5-ft-thick concrete blockhouse was placed around the target and counter. A foot of steel was substituted for the concrete in the roof and floor of the blockhouse. In addition to the blockhouse, the counter was shielded by 12 to 14 in. of paraffin, 2 in. of pressed boric acid, and 4 in. of lead. The counter's four sections were contained in 1/2-in.-thick steel boxes. The box walls along the counter axis were made of 1/32-in. aluminum sheet. The steel boxes were meant to act as the magnetic shield for the phototubes on the counter along with individual mu-metal shields and additional iron pipe shields on each photomultiplier tube. However, it was found necessary to entirely surround the aligned boxes with an additional inch of steel to completely shield the effects of the cyclotron's magnetic field.

With the total-absorption counter so shielded, the average machine background counting rate detected in the counter was 350 counts per second at full beam intensity. The pulse-height distribution of the machine background appeared to diminish exponentially with increasing pulse height, and was significant over the counter's detection range.

The lack of time correlation with target interactions allows the machine background to be reduced to about 10% of the total signal.

Cosmic radiation produced 120 counts/sec in the total-absorption counter. By use of the previously mentioned cosmic ray umbrella anti counter, the cosmic radiation counting rate was reduced to 50 counts/sec in the total-absorption counter. The pulse-height distribution due to cosmic rays has a maximum at about 85 MeV. The requirement of time correlation with target interactions reduces the cosmic ray background to 0.5% of the total signal.

d. Relative neutron-photon efficiency

The energy containment of a photon-electron shower varies markedly when the trajectory of the incident photon fails to stay within the counter for the entire length of the counter. Considering this fact and the desire to maximize the solid angle through which the total absorption counter views the target, a circular aperture 3-7/8 in. in diameter was made in the target shielding concentric to the target axis and located 40.8 in. from the target center at an angle of 83.91 deg with the incident beam line in the horizontal plane.

Since 4 in. of lead represents approximately 20 radiation lengths, the shielding is effective for photons and the counter photon efficiency ($\epsilon\gamma$) can be calculated if one knows the aperture dimensions and location, and the detection efficiency of the counter for photons.

The neutron transmission through the shielding was calculated from shielding and background studies done with a prototype total-absorption counter in the experimental area. It was found that 24 in. of paraffin attenuated the neutron spectrum from the cyclotron to 0.665 ± 0.019 of the incident spectrum. If (as assumed) the attenuation varies exponentially with thickness, the 12 in. of paraffin covering the front face of the counter would attenuate the high-energy neutron flux to 0.82 ± 0.02 of the incident spectrum. A 4-in. lead wall was erected between the target and the counter. For stopping pions the wall attenuated the detected events to 0.517 ± 0.015 of the original number. The photons represent a small fraction of the detected events and therefore the events

can be considered to be all neutrons without introducing a large error. From the shielding study data it was found that adding 12 in. of boric acid to the 4 in. of lead attenuated the neutron spectrum to 0.39 of the incident spectrum. Therefore, if (as assumed) the attenuation varies exponentially with thickness, 2 in. of boric acid would attenuate the high-energy neutron flux to 0.95±0.03 of its original value. The total effect of the shielding was to attenuate the high-energy neutron flux to 0.40±0.02 of the incident flux. Since the diameter of the counter is four times the diameter of the collimator aperture, the effective solid angle the counter subtends is 7.02 times as great for high-energy neutrons as for photons. On the basis of the efficiencies for detecting these particles in the counter, the efficiencies of the anti counters for detecting associated particles, and the relative transmission efficiencies from target to counter, the relative efficiency of the system for detecting neutrons is 2.95±0.045 times the system efficiency for detecting photons.

5. Electronics

a. Beam monitor

The logic of the electronics is illustrated by a block diagram, Fig. 8, and Table V gives information on components.

All the counters in this experiment use photomultiplier tubes to generate electrical pulses. Counters F_1 and F_2 use 6342-A phototubes powered by an exponential resistive divider. The last four stages of the divider were voltage-stabilized by replacing the resistors with Zener diodes. The beam-monitoring pulses were taken from the last dynode of the divider. The anode pulses were used for the time-of-flight measurement of beam composition.

Counters #3, #4, and dE/dx used 6810A-type phototubes. The tubes were powered by a linear resistive divider with the last four dynodes voltage-stabilized by cathode followers. The voltage was stabilized on the last dynodes to minimize gain changes due to the large currents drawn by high counting rates. Both anode and last-dynode pulses were available. The anode pulses were used to monitor the beam, and the dynode pulses were displayed on an oscilloscope.

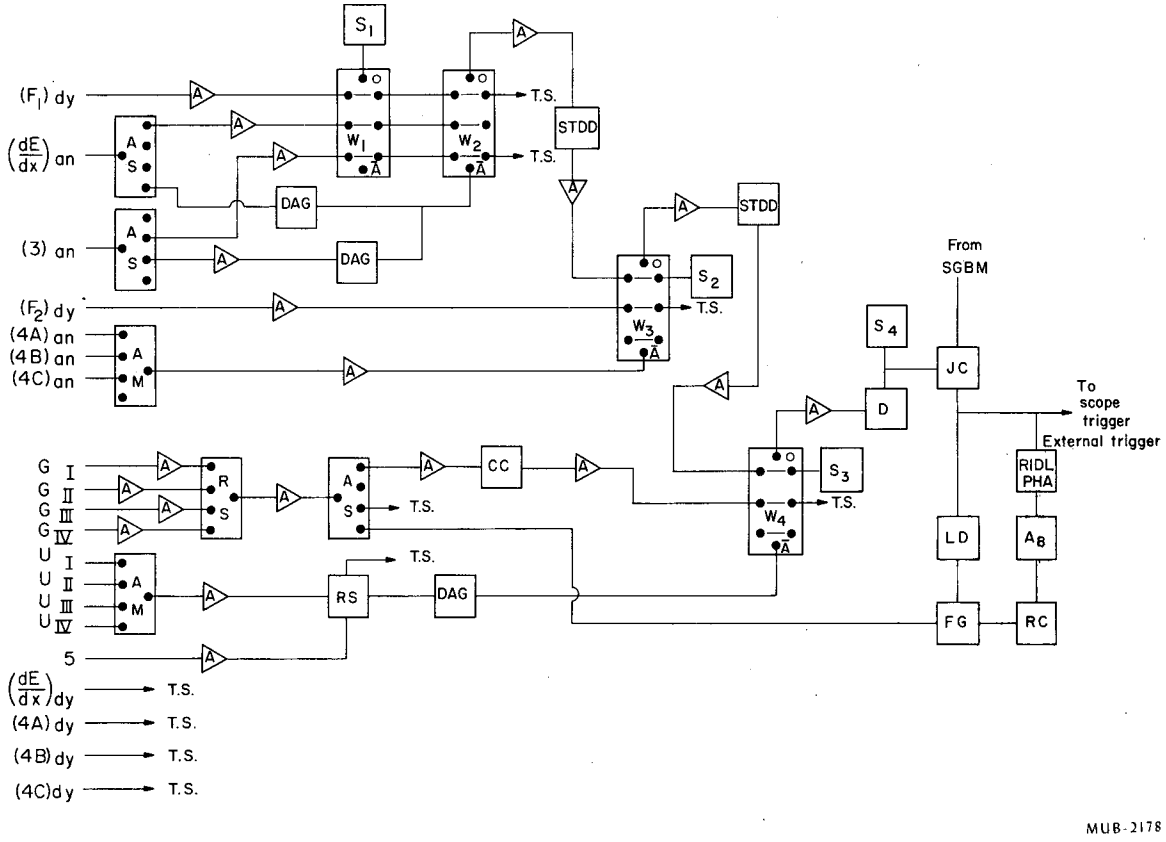

Fig. 8. A block diagram of the electronics, showing the logic. The counter signals are shown on the left with subscripts dy or an referring to dynode or anode signals where applicable. T. S. indicates "to scope" or to the four-beam oscilloscope. The component abbreviations are listed in Table V.

Table V. Electronic Equipment.

Symbol	Equipment	Remarks
A	Amplifier	Hewlett-Packard 460 AR and 460 BR
DAG	Del-A-Gate variable delay and gate	UCRL Counting Handbook, File No. CC10-5
W	Fast 3-channel coincidence and anticoincidence unit	William A. Wenzel, UCRL-8000
AS	Active splitter	UCRL Eng. Rep. EE-883
AM	Active mixer	UCRL Eng. Rep. EE-883
RS	Resistive star	n-coupling resistively matched
S	Scalers	UCRL Counting Handbook, File No. CC9-8
D	10-Mc discriminator	UCRL Counting Handbook, File CC3-11
STDD	Swift tunnel diode discriminator	David Swift (private communication), ≈ 4 nsec output
JC	"John's circuit"	Slow Rossi-type coincidence circuit (John A. Poirier, private communication)
CC	"Cordy's circuit"	See Fig. 9. Cordon Kerns (private communication)
RC	R-C pulse-stretching circuit	- - -
LD	Lipman discriminator	Norman H. Lipman (private communication), ≈ 500 nsec output, ≈ 200 nsec dead time
FG	Fast linear gate	Modification of Cal Tech linear gate CTSL-18, Barna and Marshall
A8	Linear amplifier	ORNL-2204 (1956) p. 55 and 2302, p. 48
PHA	Pulse-height analyzer	RIDL
SG BM	Scaler gate and beam monitor	Variable gate, unit triggered by cyclotron rf.

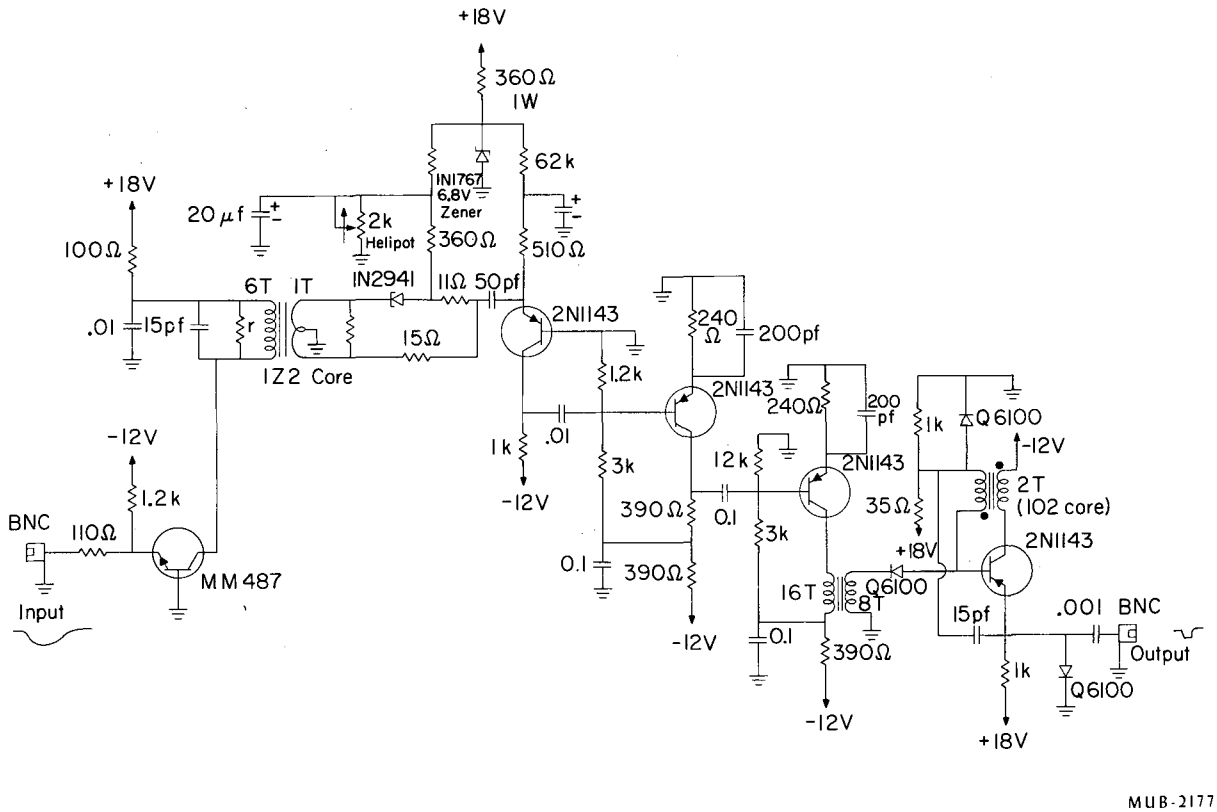

Fig. 9. This is a schematic diagram of "Cordy's circuit" or the gamma discriminator (GD), which was used to improve the timing qualities of the total absorption counter using zero crossing techniques.

The dynode signal from F_1 and the signals from dE/dx and #3 taken in coincidence in W_1 form a monitor for the total number of particles in the beam. When the 50-MeV beam was used, upper-level discriminators on dE/dx and #3 were used in anticoincidence with the above three signals in W_2 to eliminate all particles with insufficient velocity to pass completely through the target. W_2 was, then, a monitor of useful particles.

Combining W_2 in coincidence with the dynode signal from F_2 and in anticoincidence with #4A, B, C, in W_3 gave us a monitor of target interactions with neutral final states. Unfortunately, after counters #4B and #4C were made thinner there was no longer a measurable difference in the counting rate of W_3 for target full and target empty for the 50-MeV beam.

In order to improve the time resolution of the system and therefore reduce accidental events, a coincidence was made between the total-absorption counter and W_3 in anticoincidence with counters #5 and the cosmic ray umbrella anti in W_4. Since the pulse-height analyzer requires microsecond pulses, the use of a fast coincidence between W_3 and the total absorption counter of approximately 20 nanoseconds width to turn on the analyzer, rather than using W_3 alone, represents considerable improvement in the system time resolution.

b. Total absorption counter

The 6655A phototubes used on the total-absorption scintillation counter were powered by using a linear resistive divider over the first seven dynode stages of each tube, and a common high-current resistor divider powered by a separate 300-volt supply for the last three dynode stages. This arrangement allowed for individual tube gain control through separate high-voltage supplies while maintaining the voltage regulation on the last three dynodes for stabilizing the gain.

The long rise time of the pulse allowed us to tie together the anodes of the phototubes in each section at the counter. A 50-kΩ resistor provided a dc path to ground.

The signal from each section was put through an amplifier before all were added together in a resistive adder. This procedure provided a separate gain control for each section and electrically isolated each section.

The relative timing between phototubes on a given section of the counter was assumed to be the same. The relative timing of the sections was measured by timing each section on cosmic rays with an auxiliary counter placed directly over it. The timing of each section was adjusted to compensate for the flight time of a photon from one section to the next.

The added signal from the total-absorption counter was amplified and split three ways with a transistorized splitter which preserved the pulse-height information. The split signal was used for timing in W_4, used as the input to the pulse-height analyzer, and displayed on the four-beam oscilloscope.

Because the spectrum of pulses from the total absorption counter has a long rise time, any threshold sensitive device, such as most coincidence circuits, has a correspondingly large time jitter. This comes about because larger pulses attain the threshold value more quickly than small pulses. In order to improve the timing qualities of the total-absorption counter signal it was put through "Cordy's circuit." This is a circuit which differentiates the pulse and uses the differentiated pulse to fire a sensitive tunnel diode discriminator near the zero crossing point. The jitter was measured by using cosmic rays and found to be 4 nsec over the first 5% of the dynamic range of the circuit and less than 1 nsec over the remainder. The output pulse of "Cordy's circuit" was of uniform height and width. The width could be varied by a switch. There were two running conditions corresponding to a narrow output pulse of about 12 nsec (GDN) and a broad output pulse of about 24 nsec (GDB). Because of differences in the pulse shape for neutrons and photons, the difference in neutron-photon time of flight could not be considered a reliable measurement. This, however, does not affect the ability to separate by time of flight, which depends only on there being a difference in timing.

The total-absorption counter pulse that was routed to the pulse-height analyzer is sent through a linear gate which is opened for 0.5 μsec by a pulse from W_4. The linear gate reduces the effective time the analyzer is on and thus decreases the chance of pulses' piling up to give errors in the pulse-height measurement. The pulse must then be stretched in time to accommodate the input requirements of the pulse-height analyzer. The fast amplifiers that were used in the pulse-height-analyzer portion of the circuit were dc voltage supplies, in order to eliminate the gain fluctuations caused by the voltage ripple in their normal supply.

The pulse that was sent to the four-beam oscilloscope was amplified by unmodified amplifiers. The oscilloscope sweep was triggered by a pulse from W_4.

c. Accidentals and efficiencies

All the electronics was gated by a scaler gate and beam monitor. The purpose of this gate was to turn the electronics on only when there was useful beam. This eliminated problems of electrical noise from the machine itself and reduced the accidentals by eliminating the high-counting-rate portion of the beam. The cyclotron beam is spread in time, producing a useful beam which is on 50% of the time.

The number of W_2 counts indicates the number of pions incident of the target. Accidental counts in W_2 would lead to overestimating the number of pions. The measured accidental rate was 0.04%, and will be neglected.

When its anti was removed W_3 was found to track W_2 to within 96.5%. There was a count in W_4 99.15% of the time that it counted W_3 singles.

From the timing curve it was determined that W_3 was accidentally turned off by counter #4 13.3% of the time.

It was calculated that counter #5 and the cosmic ray umbrella accidentally turned off W_4 0.7% of the time.

We observed that 99.5% of the time that the pulse-height analyzer was triggered a pulse was registered.

The anti efficiency for counter #4 detecting a particle produced in association with the particle to be measured was calculated for each type of event, and appears in Table VI. For the calculation one assumes that the anti counter inefficiency is due to the statistical fluctuations in the number of photoelectrons produced by an event. Only (n, p) collisions were taken to be light-producing in the scintillator, since the carbon light-producing reactions are negligible in the energy region of most of the associated particles. The calculation was made considering averages of the possible interactions including beam profile, collisions in the target, direction of associated particles, angular variations in the anti counter of efficiency (i.e., whether the particle went through 4A or 4B), and fluctuations about the average number of photoelectrons detected in the counters. Errors were estimated from cross-section errors and dimensional uncertainties.

B. Data Analysis

The data consist of pulse-height-analyzer and film information for both 50-MeV and stopping pions in deuterium. In addition, pulse-height-analyzer data for stopping pions in hydrogen were used for the indirect measurement of the deuterium ratio. There were also available film data for 50-MeV pions in hydrogen. Since only photons were present in the 50 MeV pion-hydrogen interactions this data served as a guide to determining photon time distributions.

1. Method of Separation of Events

a. Time of flight

The measurement of the pulse-height spectrum in the total absorption counter still leaves the problem of determining whether the event was a photon or a neutron. Fortunately only the neutrons of Reaction (5) can be resolved by W_4, and these neutrons have a fixed velocity depending upon the incident pion energy. There is a difference of about 8 nsec in the time of flight from the target to the center of the first section of the total-absorption counter, for the neutrons of Reaction (5) and for the photons of Reactions (3) and (4) for stopping pions. For 50-MeV pions the time-of-flight difference is about 6 nsec.

Table VI. Calculated anti counter #4 A, B, C efficiency for detecting associated particles

Reaction	Incident pion energy (MeV)	Efficiency of anti
$\pi^- + d \rightarrow n + n$	$T_{\pi^-} = 0$	0.010±0.003
$\pi^- + d \rightarrow n + n + \gamma$	$T_{\pi^-} = 0$	0.180±0.055
$\pi^- + p \rightarrow n + \gamma$	$T_{\pi^-} = 0$	0.080±0.024
$\pi^- + d \rightarrow n + n$	$T_{\pi^-} = 50$	0.004±0.001
$\pi^- + d \rightarrow n + n + \gamma$	$T_{\pi^-} = 50$	0.101±0.030
$\pi^- + d \rightarrow \pi^0 + n + n$	$T_{\pi^-} = 50$	0.103±0.031

The time distribution, both for photons and for neutrons, tends to have an exponential character due to the variation in interaction depth in the counter, and it is further spread out by the beam profile on the target. In addition, the neutron time distribution is spread by the momentum spread of the beam and by the timing of the total-absorption counter sections relative to one another for photon rather than neutron transit times. Even so, the statistical nature of the light collection in the total-absorption counter dominates and makes the assumption of a Gaussian time distribution a reasonable one. This was borne out for large pulse heights, for which a Gaussian is a statistically good fit to the time distribution of events that are almost entirely photons. The nearly 6 nsec variance in the photon time distribution for the lowest pulse-height bin, (as will be seen in Fig. 16), shows the strong effect of the statistics.

In order to separate the photon pulse-height spectrum from the neutron pulse-height spectrum, correlated pulse-height and timing information was measured from pictures of the four beam oscilloscope traces. Plots of the time distribution were made at various pulse-height intervals. A Gaussian distribution for neutron timing and photon timing was fitted to the data in each interval by a least-squares method. The area of the Gaussian represents the number of particles at that timing and pulse-height interval.

b. Pulse-height separation

Once the photon energy spectrum has been separated from the total spectrum by a time-of-flight measurement, the problem remains of determining the relative contributions of Reactions (3) and (4). Previous measurements of the photon energy spectrum for the case of stopping pions, where only Reaction (4) contributes, show the photon energy distribution to be well defined in comparison with the resolving power of this experiment, Fig. 1. This energy peaking is in sharp contrast to the prediction according to three-body phase space and indicates a strong neutron-neutron coupling in the final state. The impulse approximation predicts no appreciable change in the spread of the energy of the

π-p system with the increase in incident pion energy. Therefore, the energy distribution of the photon from Reaction (4) should remain peaked.

Because the resolution in this experiment is broad compared with the energy spread of the photon energy distribution for Reaction (4), and because of the statistical nature of the means of measuring the photon energy, the assumption of a Gaussian for the energy distribution should be a reasonably good one.

Care was taken to ensure optimum energy resolution in recording data on the pulse-height analyzer. The data recorded on film did not share this careful treatment. A comparison of Figs. 1 and 10 indicates that the effects of gain fluctuations in the amplifiers used with the four-beam oscilloscope and film measurement uncertainties on the resolution of this method of recording the data were not negligible. For this reason and the fact that at these pulse heights only photons are present, the pulse-height-analyzer data appear to be the more useful for measuring photons from Reaction (4).

The number of Reaction (4) photons detected was taken to be equivalent to the area of a Gaussian fit to the large pulse-height events detected with the pulse-height analyzer. The π^0 photons of Reaction (3) were taken to be the remaining photons in the photon spectrum.

c. Least-squares program for fitting a sum of Gaussians

A program has been written[35] that fits a sum of Gaussians to a set of data by minimizing the function

$$Q = \sum_{i=1}^{n} W_i \left[Y(X_i) - f(X_i, a_{\ell j}) \right]^2 , \qquad (11)$$

where $Y(X_i)$ represents a set of n data points to be fitted by the function

$$f(X_i, a_{\ell j}) = \sum_{j=1}^{k} \frac{A_j}{\sqrt{2\pi}\ \sigma_j} \exp\left[-(1/2)\left(\frac{X_i - \mu_j}{\sigma_j} \right)^2 \right] \qquad (12)$$

Here the $a_{\ell j}$ ($\ell = 1, 2, 3$) correspond to the parameters of the jth Gaussian function, A_j, σ_j, μ_j, which represent the area of the jth

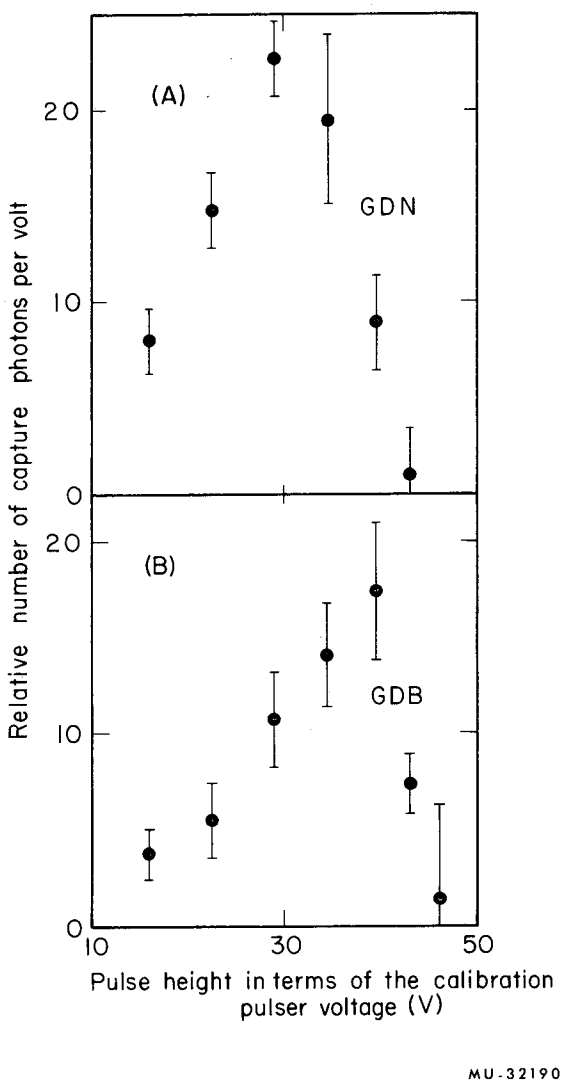

Fig. 10. The photon spectrum for radiative capture as measured by time of flight on film, plotted as a function of the amplitude of a pulser used to calibrate the system. Running condition: (A) gamma discriminator narrow, (B) gamma discriminator broad.

function, the standard deviation of the jth function, and the mean value or position of the jth function, respectively. The W_i is a weighting function which serves to stress more heavily the more accurate data. In our case W_i was taken to be the reciprocal of the square of the statistical variation of the ith data point.

Rather than calculate the parameters to be fitted directly, the program calculates corrections to an initial estimate of the parameters. To do this the program solves a matrix equation of the form $AX = Y$ for $A = YX^{-1}$. The equation is actually

$$\Delta Y_{i,0} = Y_i - f(X_i, a_{p,0})$$

$$= \sum_{k=1}^{p} \left(\frac{\partial f}{\partial a_k} \Big|_{i,0} \right) \Delta a_{k,1} \quad , \tag{13}$$

where $\left(\frac{\partial f}{\partial a_k} \Big|_{i,0} \right)$ means the partial derivative of $f(x_i, a_k)$ with respect to a_k, the kth parameter, and is evaluated at $a_{p,0}$, the initial estimates of the p parameters, at the ith data point. The $\Delta a_{k,1}$ is the first correction to the estimate of the kth parameter, and corresponds to an element of the A matrix in the form of the general equation. This calculation is repeated, using the corrected parameters as the next estimate, until the corrections are arbitrarily small.

The variance of the calculated parameters, σ_{a_k}, is given by

$$\sigma^2_{a_k} = C_{kk} \sigma^2 \quad , \tag{14}$$

where C_{kk} is the kth diagonal element of the inverse of the matrix X in the general equation. The σ^2 is the function Q divided by the number of degrees of freedom for the fit. The error in calculating a parameter by this method reflects the goodness of fit of the function to the data and the influence that particular parameter has on the fit.

Depending upon the accuracy of the initial parameter estimates and the shape of the data distribution, this calculational process may or may not converge.

It is possible to hold parameters fixed in the calculation.

2. Procedure for Separating Event Types

a. Film measurement

All counters were displayed on the four-beam oscilloscope as illustrated in Fig. 11. The pictures of the counter pulses were measured on the "Oscar." This device projects the picture on a screen where a movable cross hair can be positioned and its coordinates punched onto IBM cards. The following points were measured:

1. The position of half-maximum deflection on the leading edge of the F_1 pulse (sweep one).
2. The position of half-maximum deflection on the leading edge of the F_2 pulse (sweep one).
3 and 4. Undeflected points on sweep two.
5. The point of maximum deflection of the dE/dx pulse (sweep two).
6. An undeflected point on sweep four.
7. The position of half-maximum deflection on the leading edge of the total absorption counter pulse (sweep four).
8. The point of maximum deflection for the total absorption counter pulse (sweep four).
9. An undeflected point on sweep four.
10. The position of half-maximum deflection on the leading edge of the "Cordy's Circuit" pulse (sweep four).

These coordinates are used by the program UBERSETZ[36] to calculate beam time of flight, dE/dx pulse height, total absorption counter pulse height, and the relative timing between counter F_2 and the total absorption counter pulse using both the "Cordy's Circuit" pulse and the counter pulse itself as a time reference. The output of UBERSETZ was fed into the program SUMX,[37] which made plots of the results.

Magnification changes in the Oscar were monitored by periodic measurements of three points forming a triangle.

The operational condition of the Oscar was checked periodically by using the "point scatter" program[38] and a straight-line measurement.

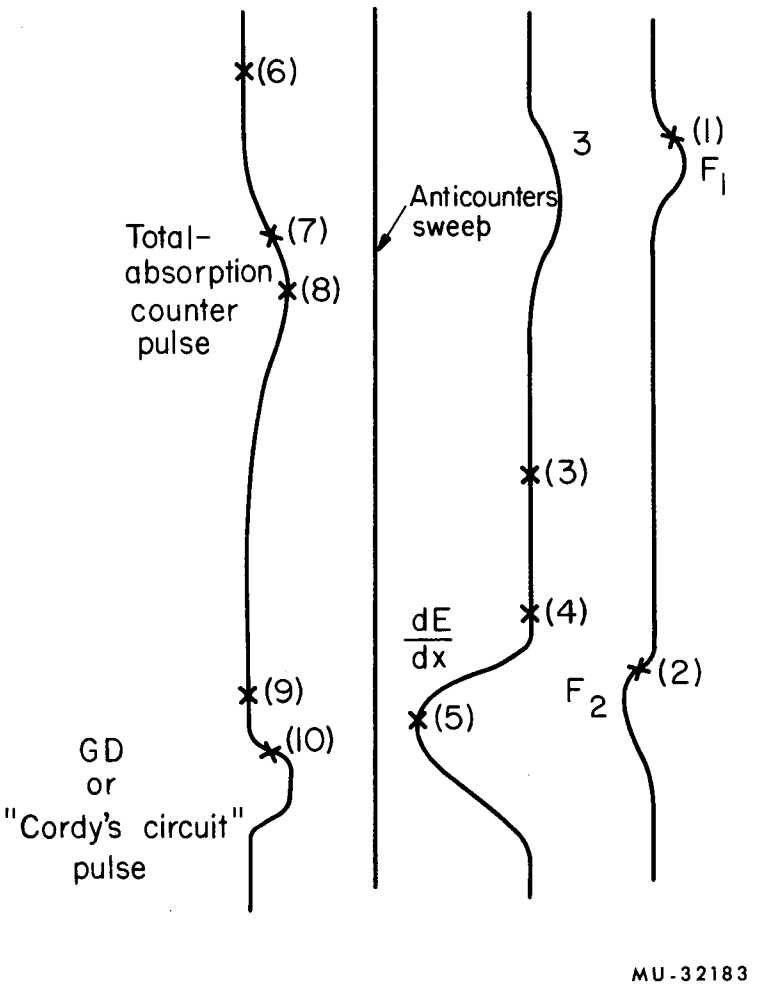

Fig. 11. Representation of a typical four-beam scope picture. The bracketed numbers show the sequence of measured points of the film.

b. Data treatment

Since the W_3 rate was the same for the target full and empty, the accidental rate was the same for the 50-MeV pion beam whether or not the target was full. This was not the case for stopping pions. However, only the condition of target full produced significant counts in the region of the photon peak.

In order to properly measure the timing distribution the relative timing efficiency for detecting events must be known. The relative timing efficiency for the film data was measured by comparing the timing distribution for stopping pion events at two different time delays. In the process a time distribution of events $f(t)$ folded with the relative timing efficiency $\epsilon(t)$ appears as the measured distribution $g_1(t)$, where

$$g_1(t) = \epsilon(t) f(t) . \tag{15}$$

A second distribution $g_2(t)$ appeared when 8 nsec delay was added to the total absorption counter signal such that

$$g_2(t) = \epsilon(t)\, f(t + 8) . \tag{16}$$

Translating $f(t + 8)$ to $f(t)$ and comparing Eqs. (15) and (16) gives the relation

$$\epsilon(t) = \frac{g_1(t)}{g_2(t-8)} \epsilon(t-8) . \tag{17}$$

The function $\epsilon(t)$ is zero everywhere except for a single region of time. As this region is approached the value of $\epsilon(t)$ increases from zero to one and remains one until the region is passed, when it decreases to zero once more. The value of $\epsilon(t)$ can be determined from the data if the function $\epsilon(t)$ or $\epsilon(t-8)$, whichever is nearer the maximum of the efficiency function, is taken to be unity. The other function can then be calculated from Eq. (17). This produces a first approximation to the efficiency function, which value may now be used for the function nearer to the maximum of the timing efficiency. This iterative procedure can be repeated until no change in the calculated efficiency results. The observed distributions $g_1(t)$ and $g_2(t)$ must be normalized to each other unless there is an even number of iterations, in which case the process

is self-normalizing. The results of this calculation, using two iterations for running conditions GDN and GDB, appear in Figs. 12 and 13.

c. Time-of-flight procedure

A glance at the time-of-flight distributions in Fig. 14 shows that there was no clear separation between photons and neutrons for the 50-MeV pion beam in deuterium. The photon time-of-flight distribution, however, can be obtained by examining the time-of-flight distribution obtained from similar conditions and use of a hydrogen target. Figure 15 shows the time distribution of photons from negative pion interactions in hydrogen. The broadening of the distribution at low pulse heights is due to poor photoelectron statistics at lower energies. Figures 16 and 17 show the variance and position of Gaussians fitted to the various timing distributions as a function of pulse height for the 50-MeV hydrogen data.

The data at large pulse heights for the deuterium target showed a 2-nsec shift in the position of photon timing distribution. This shift is undoubtedly due to slight changes in electronics during the course of the experiment such as replacement of amplifiers, tube bases, cables, etc.

Two Gaussians were fitted to the deuterium to determine the relative numbers of photons and neutrons detected. The variance of the photon Gaussian was taken to be the same as for the hydrogen data and was held fixed. The position of the photon distribution was determined from the distributions for large pulse heights. The variance of the neutron Gaussian was taken to be the same as for the photons except for the lowest pulse height, for which it was taken to be the variance of the data. The neutron variance was held fixed. Both running conditions GDN and GDB were treated in this manner.

For stopping pions there appeared to be a target-associated background. This background can best be seen on examination of Fig. 18, showing the pulse-height spectra for stopping π^- in hydrogen. The background is taken to be caused by scattered pions which are not antied and which interact in the total absorption counter shielding, producing neutrons which are detected. Evidence for scattered pions lies

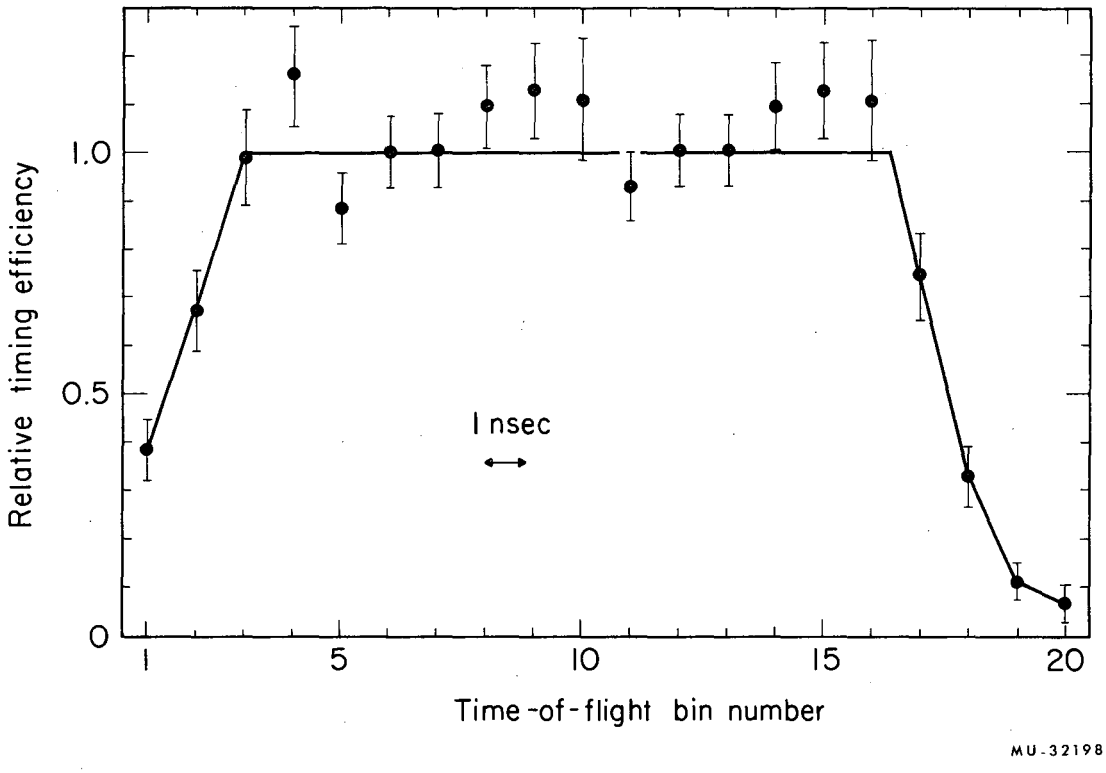

Fig. 12. Plot of the relative timing efficiency as a function of the time-of-flight timing on the film for running condition GDN.

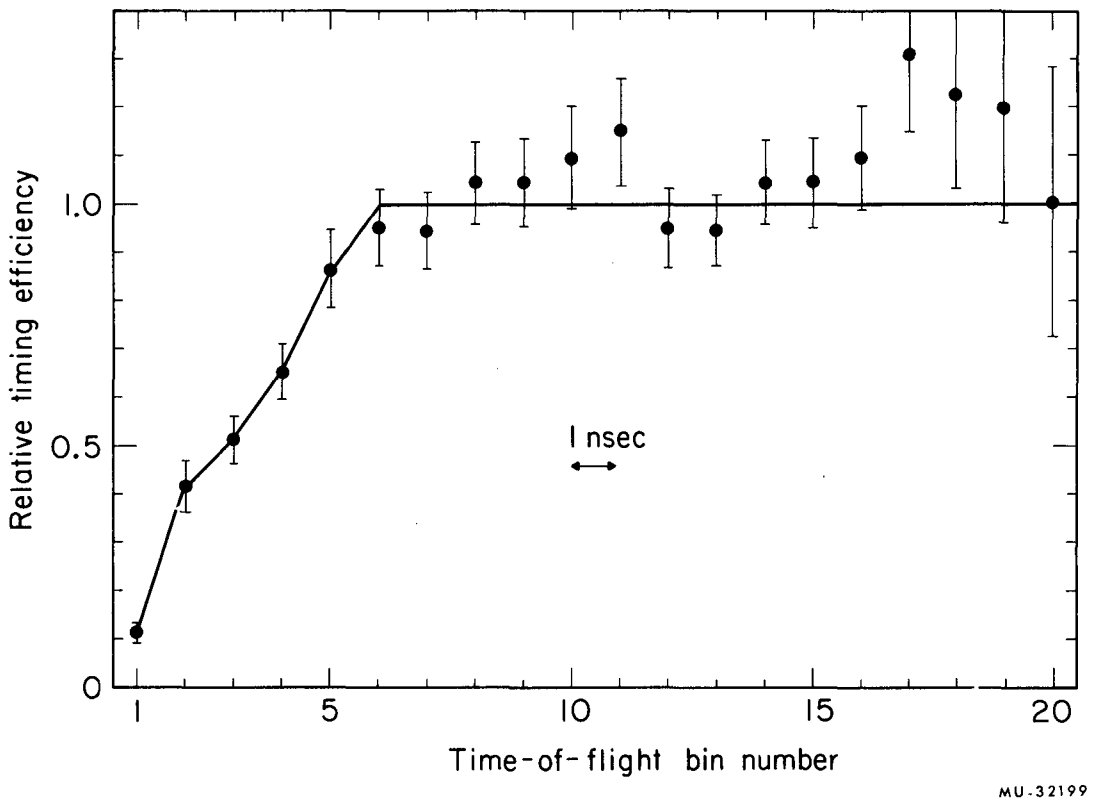

Fig. 13. Plot of the relative timing efficiency as a function of time-of-flight timing on the film for running condition GDB.

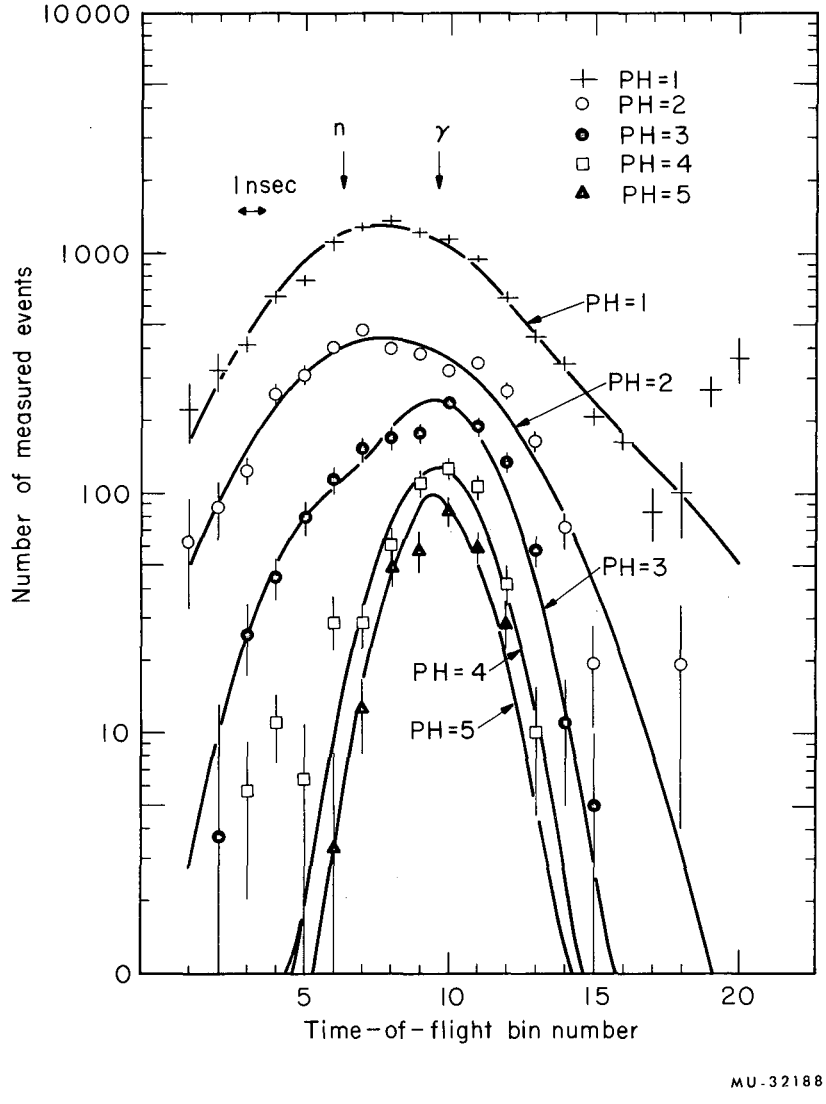

Fig. 14. Time-of-flight distributions of detected particles for 50-MeV pions on deuterium (GDN) for various pulse-height bins. The curves are the fitted Gaussians. Their center positions are indicated. Note the preponderance of neutrons at low pulse heights and their absence at high pulse heights.

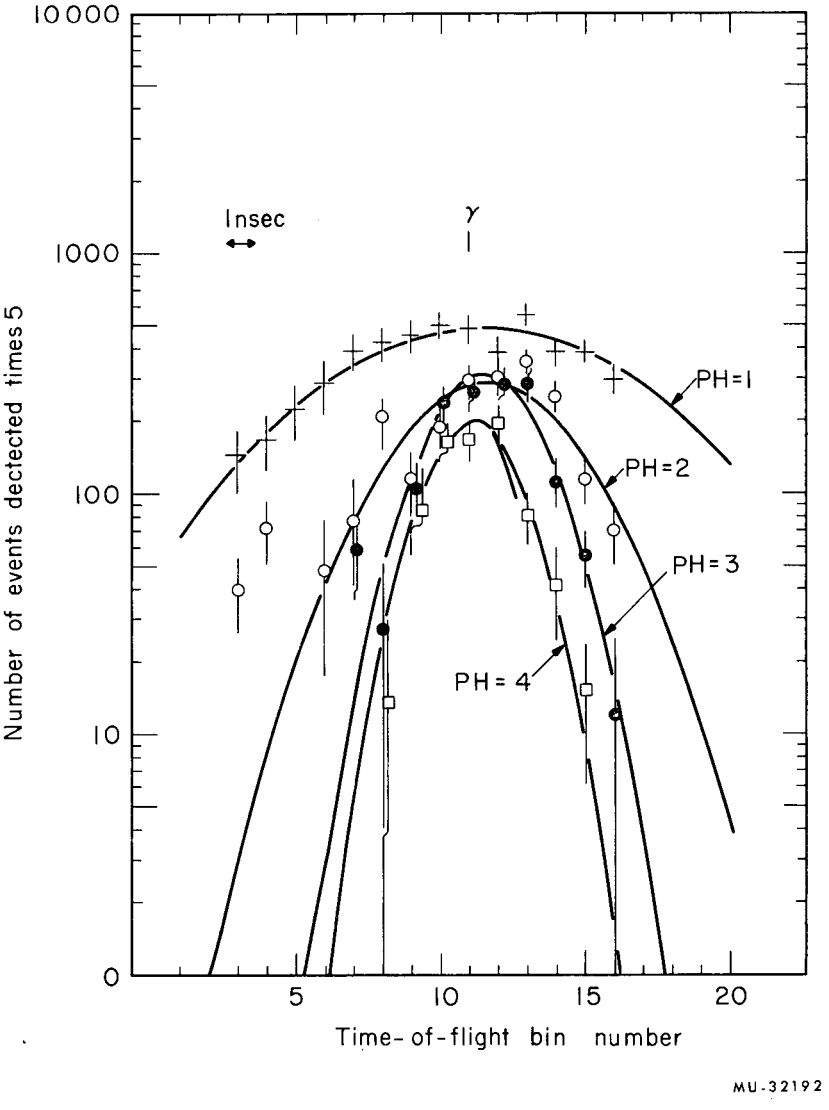

Fig. 15. Time-of-flight distribution for detected particles for 50-MeV pions on hydrogen (GDN) for various pulse-height bins. Where data points overlap the higher pulse-height bin is displaced to the right. The curves are single Gaussians fitted to the data. The data have been multiplied by five to correspond to similar numbers of incident pions, as in the deuterium case.

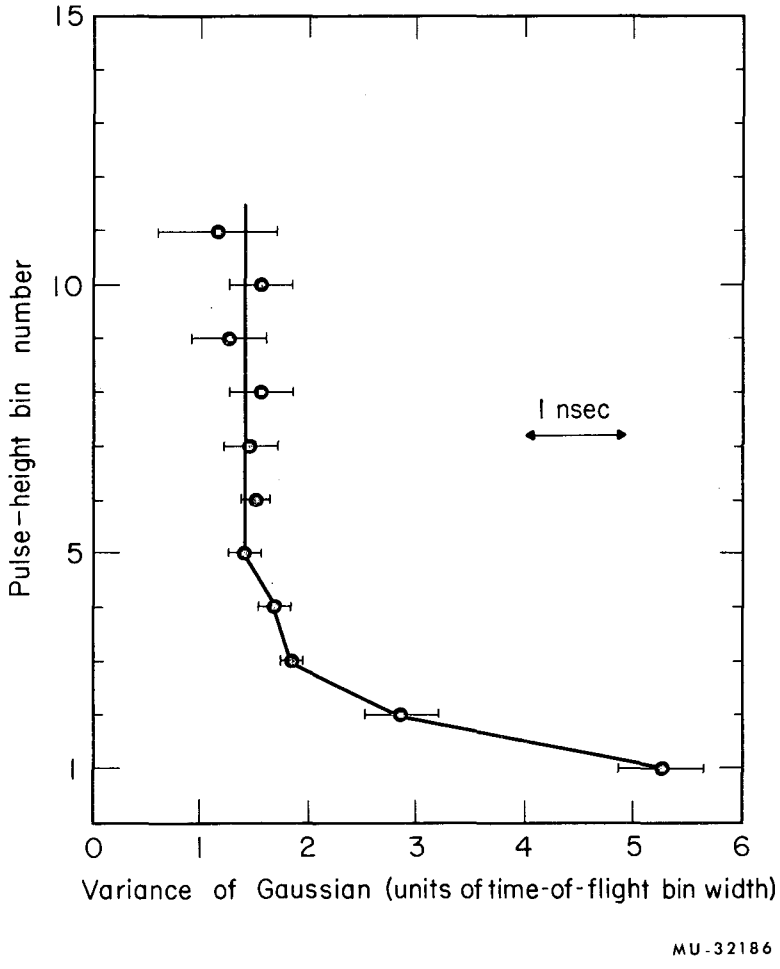

Fig. 16. Plot of the variance of the Gaussian fitted to the hydrogen data as a function of pulse-height bin. The broadening of the Gaussian at low pulse heights is a statistical effect. The solid line is the variance used in fitting deuterium data.

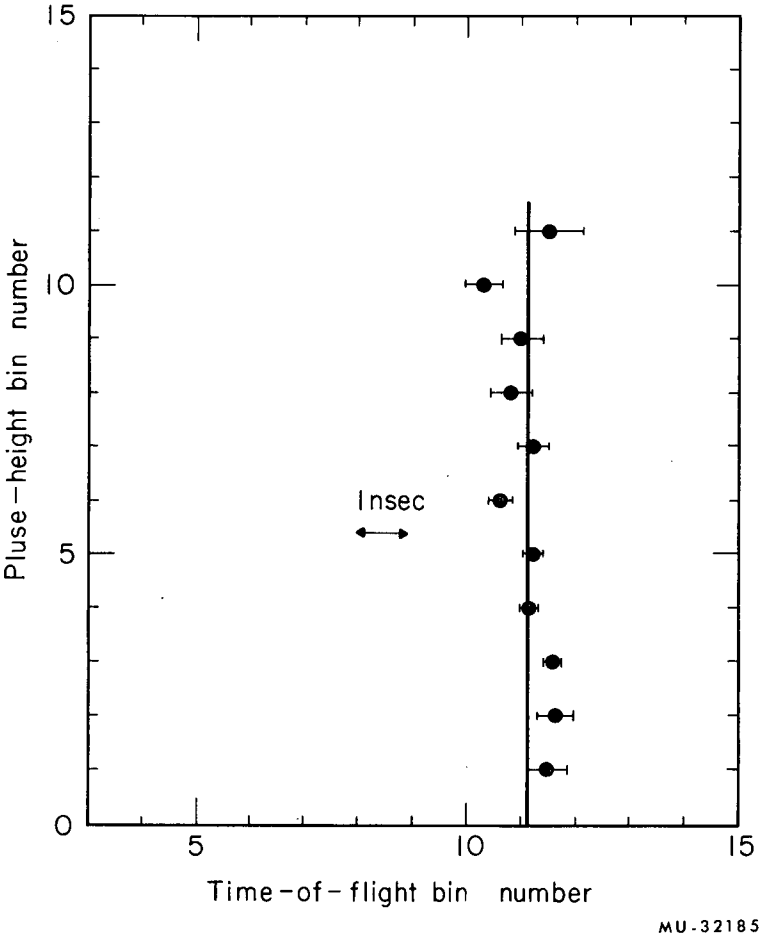

Fig. 17. Plot of the position of the Gaussian fitted to the hydrogen data as a function of pulse-height bin. It appears to be consistent with the straight line drawn through the data.

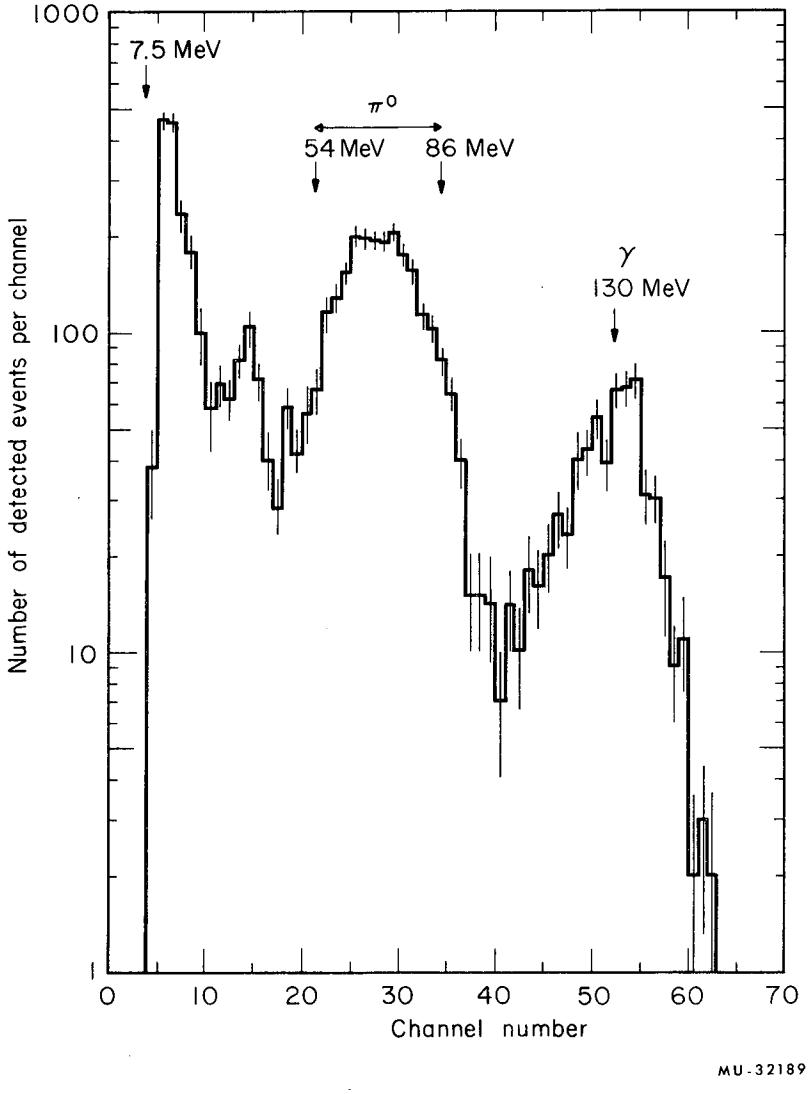

Fig. 18. The pulse-height distribution of detected particles for stopping pions in hydrogen plotted as a function of channel number in the pulse-height analyzer. The distributions of radiative-capture photons and charge-exchange capture photons are indicated. The existence of a background predominantly at low pulse heights is apparent.

in the observation of charged particles from the target in anti counter #5 when it is removed from the circuitry but still displayed on the oscilloscope. Evidence against photons is that when a 1/4-in. lead converter is placed over the collimator aperture under these running conditions, no more than the expected number of pairs is observed. Further evidence lies in the similarity of the timing distributions of the background and the target-empty events for stopping π^- in deuterium, as illustrated in Figs. 19 and 20. This target-associated background was neglected at 50 MeV. Unantied scattering off the empty target at 50 MeV was so great the effect of scattering off the deuterium was lost. This was illustrated by our inability to measure the neutral cross section with the counter telescope (W_3).

For stopping π^- in deuterium the target-associated background was included in fitting the timing distributions, and was taken to have the same shape as the target-empty events. The neutron distribution was assumed to have the same variance as was found for the 50-MeV data, and was held fixed.

The final determination of the number of photons, neutrons, and target background events at each pulse height in deuterium was taken to be the area of each respective Gaussian determined by the fit, Table VII. The errors reflect the accuracy of the Gaussian assumption in that they include the goodness of fit in their evaluation. That this method is actually a means of dividing the data between the possible events and does not alter the total number of events at a given pulse height is illustrated in Table VIII.

d. Procedure for determining the area of the photon peak

Since the pulse-height analyzer data have the better pulse-height resolution, those were the data used to determine photon peak area. The photon peak area represents the number of Reaction (4) events detected.

For stopping pions the photon peak is clearly resolved and was fitted by a single Gaussian by considering the data within seven channels of the peak maximum. The contribution from other sources in this energy region was assumed negligible. This procedure was used for

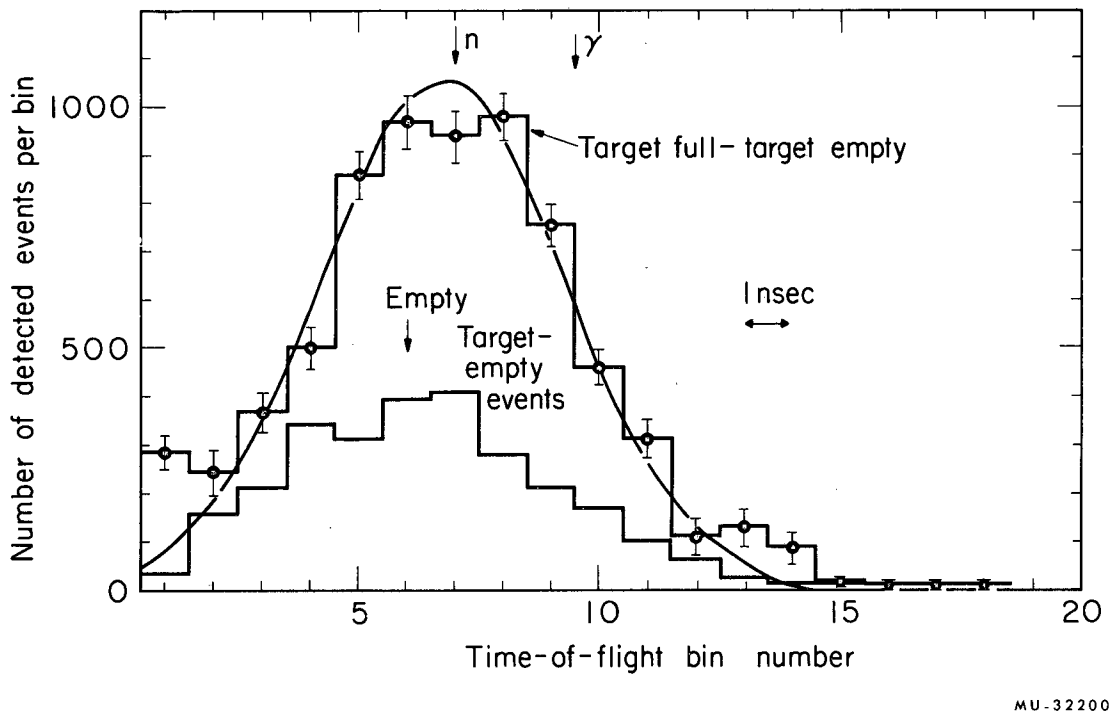

Fig. 19. The time-of-flight distribution of detected particles in the lowest pulse-height bin plotted for stopping pions in deuterium (GDN). The target-empty events are indicated and have been shown for comparable numbers of incident particles. The curve is a two-Gaussian fit. Arrows indicate central positions of timing distributions.

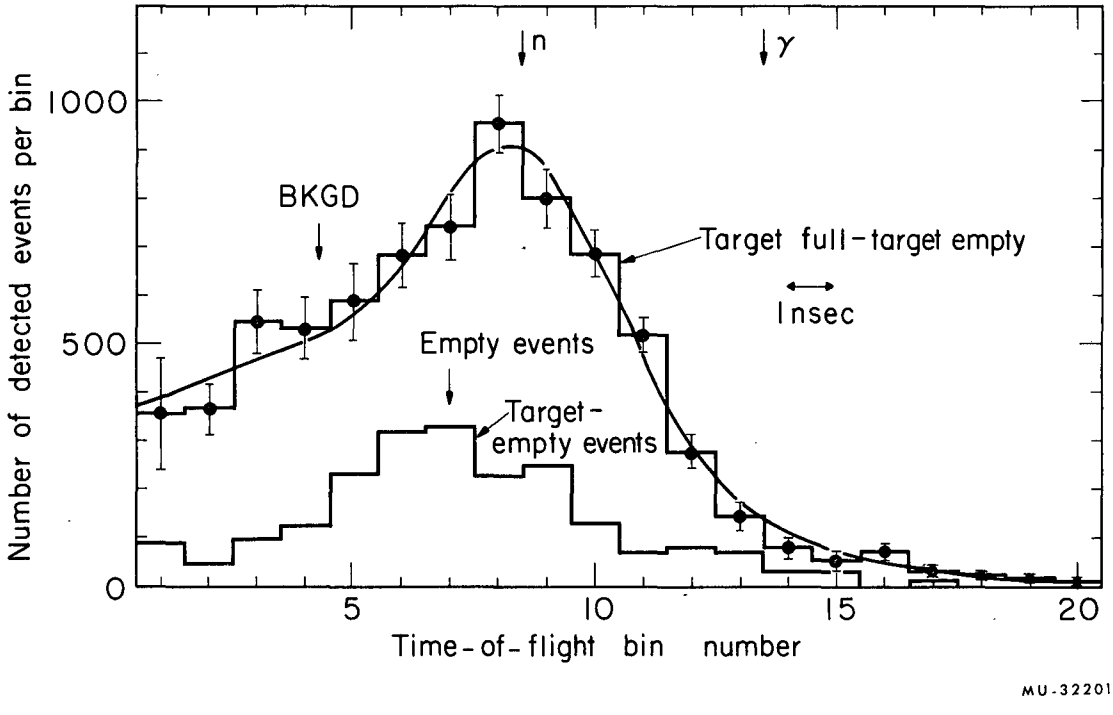

Fig. 20. The time-of-flight distribution of detected particles in the lowest pulse-height bin plotted for stopping pions in deuterium (GDB). The target-empty events have been shown for comparable numbers of incident particles. The difference in position for background and target-empty events, which was not apparent for GDN, is a combination of the energy loss in the target and shifting of the distribution toward the center of the timing efficiency curve. The curve is a two-Gaussian fit. The change in separation of the neutron and photon time of flight compared with the preceding figure is an electronic effect.

Table VII. Spectra separated by time of flight

	GDN		GDB	
	2.371×10^9 pions		525.2×10^6 pions	
Pulse-height bins	Photons	Neutrons	Photons	Neutrons
At T_π = 50 MeV				
1	4045±412	7888±426	631.8±85.6	2075±106
2	1723±313	2012±298	107.6±49.2	523.7±64.4
3	1074±72	330.7±56.1	147.5±20.9	169.5±24.1
4	504.5±41.9	-	115.0±25.7	-
5	305.7±18.8	-	75.9±11.3	-
6	171.9±21.3	-	36.2±11.4	-
7	87.2±13.0	-	24.9± 8.0	-
8	74.0±12.2	-	14.1± 5.8	-
9	53.0±10.8	-	6.7± 6.9	-
10	17.8± 8.8	-	8.8± 4.8	-
11	2.7± 5.6	-	4.5± 6.0	-
12	2.6± 6.4	-	2.3± 6.7	-
13	1.3± 5.9	-	2.6± 8.5	-
Total	8,062.7±525	10,230.7±522	1,177.9±107	2,768.2±126.5

Table VII. (continued)

Pulse-height bins	GDN			GDB		
	Photons	Neutrons	Background	Photons	Neutron	Background
At T_π = 0 MeV						
1	-	5111±804	1594±817	-	2632±719	6448±511
2	-	890±113.4	69.5 ±125.9	-	840.9±78.4	666.6±68.0
3	54.4±12.2	67.2 ±31.4	59.4± 21.8	25.8± 9.3	160.8±18.1	14.8±12.7
4	98.7±13.4	-	-	36.4±13.4	-	-
5	138.5±12.0	-	-	65.8±15.0	-	-
6	101.6±24.3	-	-	73.7±14.2	-	-
7	37.9±11.0	-	-	73.2±15.3	-	-
8	3.4± 9.1	-	-	25.0± 5.6	-	-
9	-	-	-	3.6±13.6	-	-
10	-	-	-	-	-	-
11	-	-	-	-	-	-
12	-	-	-	-	-	-
13	-	-	-	-	-	-
Total	434.5±35.6	6068.2±813	1722.9±826	303.5±33.8	3,633.7±723	7129±515

Table VIII. Comparison of experimental data (number of events) with the sum of the areas of Gaussians fitted to the data

Pulse-height bin	Data	$\Sigma A_{Gaussian}$
1	12,180±316	11,933±592
2	3,739±126	3,735±432
3	1,424± 71	1,405± 91
4	541.6 ±72.8	504.5 ± 41.9
5	292.0 ±57.9	305.7 ± 18.8
6	183.0 ±29.6	171.9 ± 21.3
7	107.2 ±24.9	87.2 ± 13.0
8	96.55±23.2	74.0 ± 12.2
9	73.57±19.3	53.0 ± 10.8
10	39.39±12.0	17.8 ± 8.8
11	1.254 ± 4.92	2.7 ± 5.6
12	-3.021 ± 7.4	2.6 ± 6.4

both hydrogen and deuterium data and represents a measurement of the resolving power of the apparatus in the case of hydrogen (Fig. 21).

The photon peak in deuterium is no longer clearly resolved for 50-MeV pions (Fig. 22). The contribution in this energy region from other sources can no longer be neglected. These outside contributions were approximated by the wing of a Gaussian located outside the region of interest and below the photon peak. Only data in the region of the peak were considered. The variance (i.e., spread) of the distribution due to outside sources was allowed to vary. Since the variance of the photon peak if allowed to vary became smaller than the resolution of the apparatus could possibly allow, the variance of the photon peak was held fixed. The photon variance was taken to be the resolution of the stopping pion photon peak. The resolution was assumed to be limited by photoelectron statistics. Therefore, the variance was assumed to be proportional to the square root of the energy of the photon peak. Evidence to support this assumption lies in the finding that the total-absorption counter was affected only 3% by the change in position in the counter of detected events, and that increasing the light-collection efficiency of the counter improved the resolution.

C. Results

1. Deuterium Ratio

a. The method

When a large number, N, of negative pions stop in deuterium they react either through Reaction (4) or Reaction (5) to produce $\#\gamma_D$ photons and #n fast neutrons by the respective reactions. The relationship between N, $\#\gamma_D$, and #n can be written as

$$N = (\#n/2)+\#\gamma_D \quad . \quad (18)$$

If the same number of negative pions stop in hydrogen they undergo either Reaction (10) or the charge-exchange reaction,

$$\pi^- + p \rightarrow \pi^0 + n \ , \quad (19)$$

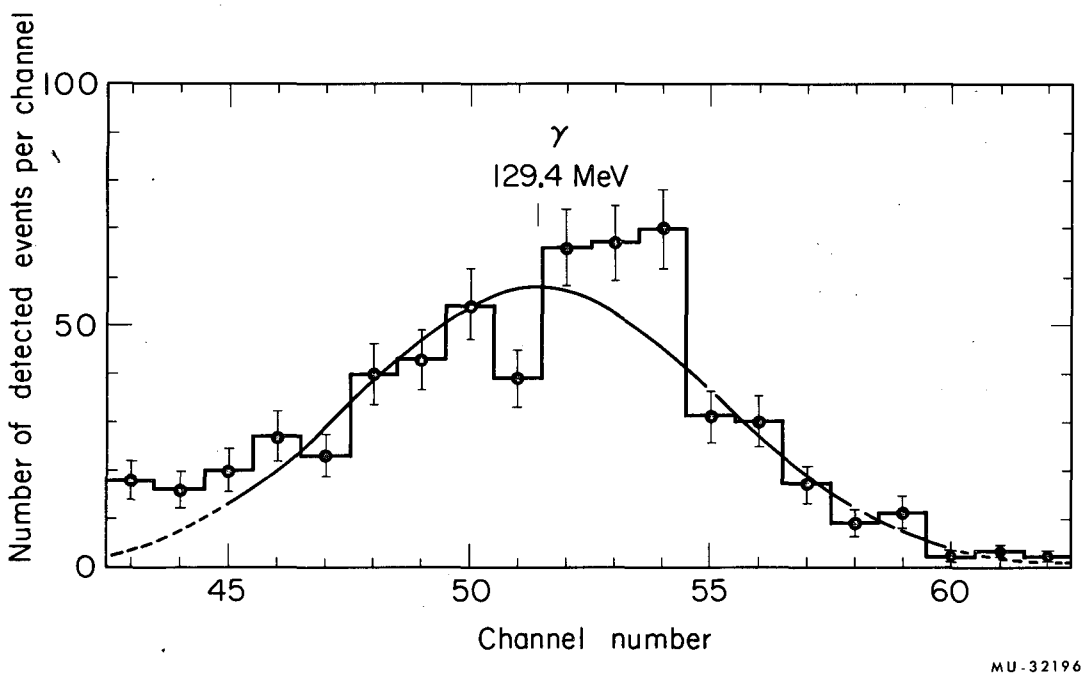

Fig. 21. Plot of the radiative-capture photon energy distribution in hydrogen as a function of channel number in the pulse-height analyzer used. The Gaussian fit to this distribution shows the energy resolution of the system to be (8.6±0.6)% half width at half maximum.

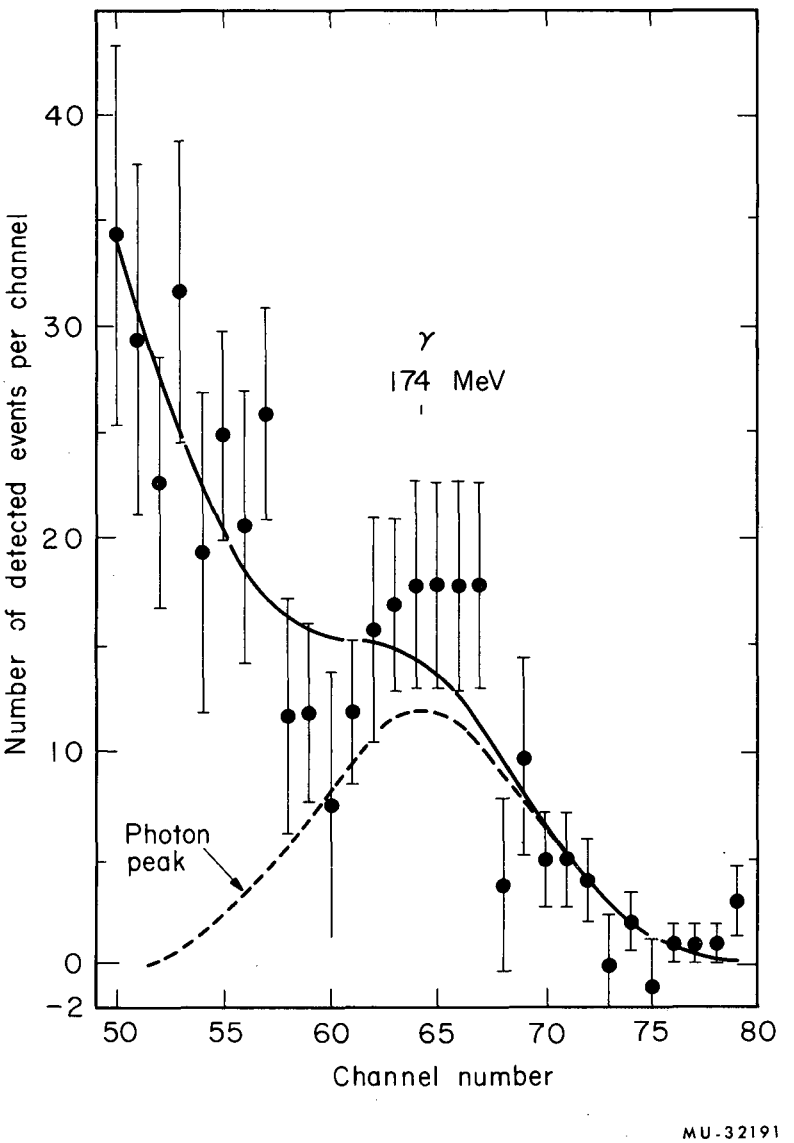

Fig. 22. The high-energy portion of the total-absorption counter spectrum for 50-MeV pion on deuterium (GDN) shown as a function of channel number in the pulse-height analyzer. The Gaussians fitted to the data are shown, and indicate 151.3±44.6 radiative absorption photons for 2.233×10^{9} incident pions.

to produce $\#\gamma_H$ photons and $\#\pi^0$ neutral pions. The relationship of N, $\#\gamma_H$, and $\#\pi^0$ can be written as

$$N = \#\pi^0 + \#\gamma_H . \tag{20}$$

The Panofsky ratio, P, can be expressed as

$$P = \#\pi^0/\#\gamma_H , \tag{21}$$

and the deuterium ratio, S, as

$$S = \#n/2\ \#\gamma_D . \tag{22}$$

Combining Eqs. (18), (20), (21), and (22), we obtain

$$N = (P + 1)\ \#\gamma_H = (S + 1)\ \#\gamma_D$$

or

$$S = (P + 1)\ (\#\gamma_H/\#\gamma_D) - 1 . \tag{9}$$

Therefore to measure the deuterium ratio, S, it is necessary to know the Panofsky ratio, P, and the ratio of radiative capture photons produced in hydrogen and deuterium per stopping pion.

b. The measurement

The number of negative pions stopping in the target was taken to be proportional to the number of W_3 counts. This proportionality should be the same for hydrogen and deuterium except for the effect on the efficiency of the anti of the difference in scattering cross sections for hydrogen and deuterium. The maximum effect this can have has been calculated to be less than 1% assuming a scattering cross section difference of 10 mb and an isotropic angular distribution. This effect has therefore been neglected.

The efficiency for detecting the photons from hydrogen and deuterium is the same except for the difference in the efficiency of counter #4 for detecting the associated neutrons and anti-ing the event. These efficiencies were discussed previously.

The numbers of photons detected were taken to be the areas of the Gaussian fit to the respective pulse-height distributions shown in Figs. 1 and 22.

The Panofsky ratio was taken to be the weighted average appearing in Table II.

2. 50-MeV Cross Sections

The cross sections to be determined can be expressed as

$$\sigma = \frac{(\#\text{D. E.})\, A_d}{(\text{Multiplicity of events})\, \#\pi\, \rho_d \epsilon \cdot (t\Omega)\, (6.0228 \pm 0.0011) \times 10^{23}} \cdot \tag{23}$$

where #D. E. = the number of detected events obtained as previously discussed,

A_d = the atomic weight of deuterium,[39]

Multiplicity of events mean the number of detectable particles produced in a single reaction [i. e., one for Reaction (4) and two for either Reaction (3) or (5)],

$\#\pi$ = the number of pions incident on the target. This was obtained by summing the products of the measured beam composition and their correlative W_2 counts for all the appropriate runs,

ρ_d = the density of deuterium,

ϵ = the combined detection efficiency. This includes the percent live time due to accidental antis, the various electronic efficiencies, the efficiency of the total absorption counter for detecting a photon, the probability that a photon before it reaches the counter may produce an electron that would anti the event, the efficiency of the anti counters for detecting associated particles produced in the reaction, and in the case of neutrons the relative neutron-photon detection efficiency,

$$(t\Omega) = \frac{\int \text{beam profile } (t\Omega) dS}{\int \text{beam profile } dS},$$

this is, the target thickness t times the solid angle Ω that the detector subtends in the center of mass of the reaction integrated over the normalized beam profile on the target.

The resultant cross sections are given in Table IX.

Table IX. Results

Reaction	Condition		Cross section at 90 deg c.m. and T_{π^-} = 50 MeV (cm^2/sr)
$\pi^- + d \rightarrow n + n + \gamma$	GDN		$(3.366 \pm 1.017) \times 10^{-29}$
	GDB		$(2.992 \pm 0.871) \times 10^{-29}$
		Weighted average	$(3.167 \pm 0.660) \times 10^{-29}$
$\pi^- + d \rightarrow n + n$	GDN		$(2.817 \pm 0.485) \times 10^{-28}$
	GDB		$(3.438 \pm 0.588) \times 10^{-28}$
		Weighted average	$(3.068 \pm 0.375) \times 10^{-28}$
$\pi^- + d \rightarrow \pi^0 + n + n$	GDN		$(8.32 \pm 0.77) \times 10^{-28}$
	GDB		$(5.44 \pm 0.61) \times 10^{-28}$
		Weighted average	$(6.56 \pm 0.48) \times 10^{-28}$

Method	Condition		Deuterium ratio
Comparison of radiative-capture peaks (P = 1.534±0.018)			3.37±0.46
Direct detection of both reactions	GDN		2.05±0.45
	GDB		1.76±0.49
		Weighted average	1.92±0.33
Comparison of cross sections for 50 MeV	GDN		1.38±0.52
	GDB		1.69±0.62
		Weighted average	1.51±0.40

3. Errors

The errors in the results include the variance of fit parameters and reflect the accuracy of the various fit assumptions, as is illustrated by Eq. (14). This type of error appears in the number of detected events and the number of pions incident on the target. Errors in the target density come from uncertainty in target vapor pressure and therefore from uncertainty in temperature and density. In addition the estimate of the fraction of the target volume that is gas (due to boiling) has been included in the density error. The errors in the atomic weight and in Avogadro's number are their quoted errors. All other errors are derived from statistical variance of measured numbers, dimensional uncertainties, and errors in cross sections used in correctional calculations.

III. SUMMARY

It was the purpose of this experiment to measure the following cross sections and relations: the deuterium ratio,

$$S = \frac{\omega(\pi^- + d \rightarrow n + n)}{\omega(\pi^- + d \rightarrow n + n + \gamma)} , \tag{7}$$

$$\sigma(\pi^- + d \rightarrow \pi^0 + n + n) , \tag{24}$$

$$\sigma(\pi^- + d \rightarrow n + n + \gamma) , \tag{25}$$

$$\sigma(\pi^- + d \rightarrow n + n) . \tag{26}$$

The cross sections were measured at a pion energy of 50 MeV in the laboratory system and an angle of 90 deg in the center-of-mass system. It was hoped that discrepancies in the deuterium branch of the s-wave pion relations in Table I could be resolved through measurement of intermediate steps in the chain of relations. In particular we hope to obtain a more direct verification of the ratio of radiative capture in deuterium and hydrogen,

$$T = \frac{\omega(\pi^- + d \rightarrow n + n + \gamma)}{\omega(\pi^- + p \rightarrow n + \gamma)} . \tag{8}$$

The measurements were carried out with a total-absorption scintillation counter to measure the photon energy spectrum produced in a deuterium target by incident negative pions and to detect the fast neutrons of Reaction (5). The data were recorded by using a pulse-height analyzer and by taking pictures of all of the counters' pulses on a four-beam oscilloscope. Since the pulse-height analyzer had considerably better pulse-height resolution than the film measurements, the pulse-height analyzer data were used in the separation of the relatively monoenergetic photon peak of Reaction (4). The film data were used to separate the neutron, photon, and target background spectra by means of the relative time-of-flight and correlated pulse-height information it affords. The spectra were separated by fitting three Gaussians to the relative timing distribution at each pulse-height interval.

The deuterium ratio was measured by fitting a Gaussian to the photon peak in the measured photon spectra for stopping π's in hydrogen and deuterium and using the areas of these Gaussians in Eq. (9) to calculate the results.

A direct measurement of the deuterium ratio was obtained by using Eq. (22). The number of neutrons used was the total number of neutrons in the neutron pulse-height spectrum determined from the film data scaled by the relative efficiency for detecting neutrons and photons. The number of photons was taken to be the sum of the photons in the photon spectrum determined from the film data.

The cross section (26) was measured by adding all the neutrons in the neutron spectrum and using this number in Eq. (23). Cross section (25) was measured by fitting a Gaussian with the variance of the detector resolution to the pulse-height analyzer data, determining its area, and using this number in Eq. (23). The number of π^0 photons detected was taken to be the difference between the total number of photons in the photon spectrum and the area of the photon peak.

The results are summarized in Table IX.

IV. CONCLUSIONS

There are not sufficient data in this experiment to determine the s-wave contributions to the measured cross sections. However, if the radiative absorption cross section at $T_\pi = 50$ MeV is taken to be entirely s-wave, it is in good agreement with the value of T calculated by Traxler, as can be seen from Table IV. The large variation in values for T in Table IV appears to be due to the variation in the measured deuterium ratio. Examination of Table III shows a consistent discrepancy between the value of the deuterium ratio obtained by the method of comparing the radiative-capture photons in hydrogen and deuterium and the value obtained by direct detection of both reactions. Since the value of the deuterium ratio measured by direct detection methods agrees with the calculated value from the measured cross sections and from the s-wave relations, I believe this to be the true value. The weighted average of the directly measured deuterium ratio and the value calculated from the cross-section measurements is $S = 1.73 \pm 0.24$, compared to the value calculated by the s-wave pion relations of $S = 1.74 \pm 0.26$.

I believe the discrepancy in measurements obtained by comparison of radiative-capture photons comes about in the following way:

If N beam particles are incident on a hydrogen target, N_{π^0} of these particles capture and produce neutral pions, $N_{\gamma H}$ of these capture and produce photons, and N_H do neither of these because they either are not pions, or scatter out of the target, or pass through the target without stopping. Therefore

$$N = N_{\pi^0} + N_{\gamma H} + N_H . \tag{27}$$

Similarly, of N beam particles incident on a deuterium target N_n produce neutrons only, $N_{\gamma D}$ produce photons, and N_D do neither for the same reasons. Using the definitions of the Panofsky ratio and the deuterium ratio, one can show that the deuterium ratio can be expressed as

$$S = (P + 1) \frac{N_{\gamma H}}{N_{\gamma D}} - 1 + \frac{N_H - N_D}{N_{\gamma D}} . \tag{28}$$

The beam composition was the same for both hydrogen and deuterium, and this effect cancels itself out. In the pair-spectrometer experiments only the incident beam was monitored and a correction was applied for the difference in pion range in hydrogen and deuterium. This correction would have the greater fraction of pions stopping in deuterium. The direct detection methods used in this experiment indicate 12.4% of the beam was captured in hydrogen while only 5.6% of the beam was captured in deuterium. The reason for the difference appears to be the difference in pions scattered out of the target. The scattered pions produce the observed target-associated background. The efficiency of the anti counter system used in this experiment was strongly dependent on the scattering angle of the nonneutral interacting beam particles. The fraction of true captures to apparent captures was 0.54 for hydrogen and 0.35 for deuterium, indicating that a greater fraction of beam particles scatters through the inefficient portions of the anti counter for deuterium than for hydrogen. It is to be expected that the effect of loss due to scattering is strongly a function of target geometry. The target with the dimension along the beam line greater than the dimension normal to the beam line loses more particles because of scattering. This correction is particularly significant when a large fraction of the beam is expected to stop in the target. Examination of the target geometry in the previous pair-spectrometer experiments shows this ratio, length along the beam to diameter normal to the beam, to be 2-1/2 for Panofsky's gas target, 1-2/3 for Ryan's liquid target, and 1 for Kuehner's liquid target, which was spherical.

Since the s-wave contribution to Reaction (5) is not measured in this experiment, the transition rate for that reaction is obtained by comparison of the cross section with the charge-symmetric case. Durbin, Loar, and Steinberger measured the cross section for the reaction $\pi^+ + d \rightarrow p + p$ near the incident pion energy of 50 MeV.[40] They found the cross section could be expressed as $18(\cos^2\theta + 0.2)\times 10^{-28}$ cm^2/sr, yielding a total cross section of 6.1±0.6 mb. At 90 deg in the center-of-mass system their measurement gives $(3.6\pm0.4)\times 10^{-28}$ cm^2/sr, compared

to our measurement of $(3.67\pm0.45)\times10^{-28}$ cm^2/sr for the reaction $\pi^- + d \rightarrow n + n$. The capture rate for Reaction (5) is calculated in the s-wave pion relations from data on the inverse charge-symmetric reaction; this calculated value can be scaled by the ratio of these measured cross sections to give the capture rate indicated by our measurement.

A comparison of our measured value of (9.84±0.72) mb for the charge-exchange cross section in deuterium with the same reaction in hydrogen (Fig. 23) shows that the impulse approximation is a good one and that the s-wave contribution is no longer inhibited by the available energy. A comparison with the data of Roberts and Tinlot,[41] who found the deuterium charge-exchange cross section to be one-third of the hydrogen charge-exchange cross section at $T_{\pi^-} = 34$ MeV, indicates that Reaction (3) ceases to be inhibited by insufficient energy between 34 and 50 MeV incident pion energy.

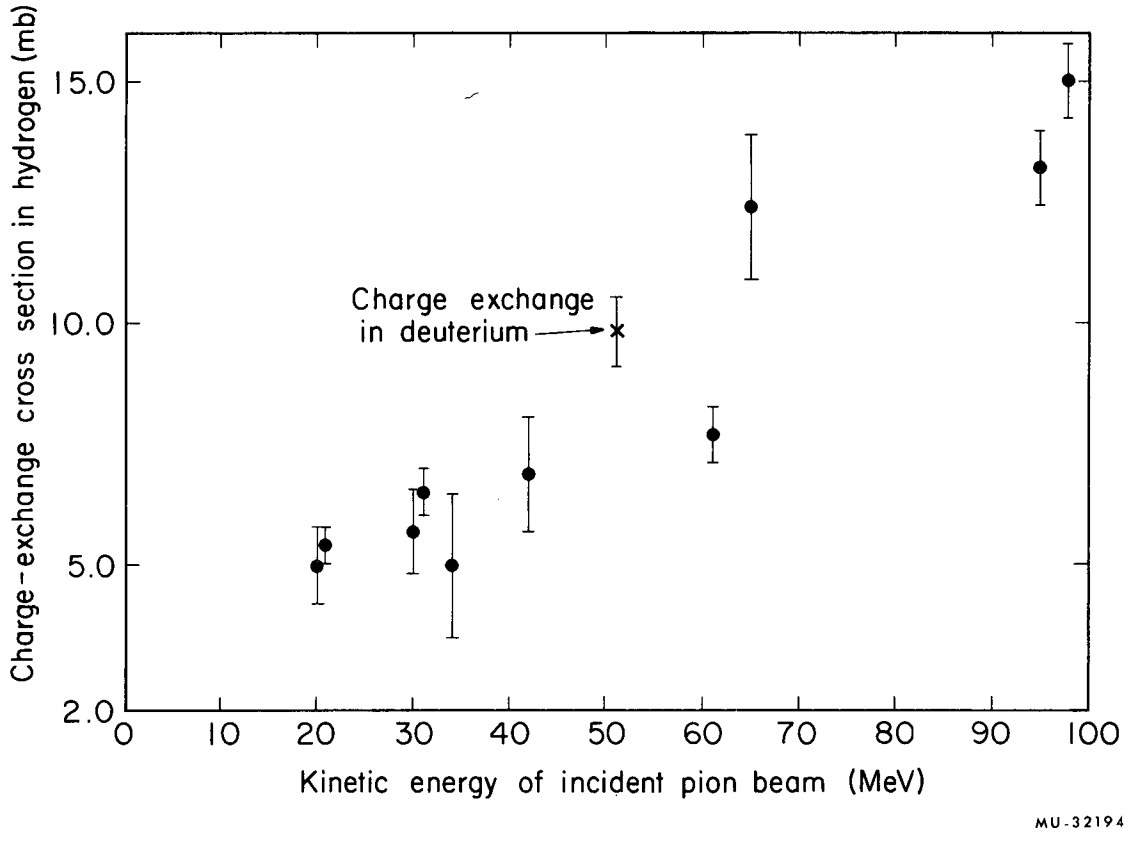

Fig. 23. The hydrogen charge-exchange cross section plotted as a function of incident pion energy. The deuterium charge-exchange cross section measured by this experiment is compared. The cross sections, in order of increasing energy, were measured by Spry (reference 42), Miyake et al. (reference 43), Spry, Miyake et al., Tinlot et al. (reference 41), Tinlot et al. (reference 44), Spry,[42] this experiment, York et al. (reference 45), Bodansky et al.,(reference 46), York et al., and Edwards et al. (reference 47).

ACKNOWLEDGMENTS

I am indebted to Dr. Robert W. Kenney and Dr. John A. Poirier, who suggested this topic and were of invaluable assistance throughout the experiment. Heartfelt thanks go to Mr. Jim B. Carroll, who collaborated with me on many phases of this work. I am grateful to Professor Burton J. Moyer for the many helpful suggestions he has given me in our numerous discussions. I want to thank Dr. Morris Pripstein for his help in designing the beam and Dr. Thomas J. Devlin, Jr., for his assistance during the final run.

I would like to acknowledge the efforts of Jimmy Vale and his cyclotron crew, my scanners, and the many experimental support groups at the Laboratory.

I want to express my appreciation to Miss Miriam Machlis for typing my thesis.

My sincere gratitude goes to my wife, Betty, whose patience and encouragement have been an inspiration to me.

This work was done under the auspices of the U. S. Atomic Energy Commission.

APPENDIX

s-Wave Pion Relations

The cross sections for production reactions such as $p + p \rightarrow \pi^+ + d$ are characterized by an $\eta^{(2\ell+1)}$ dependence in terms of the center-of-mass momentum of the final-state particles in units of $m_\pi c$, η, and their relative angular momentum, ℓ. Crawford and Stevenson determined the total cross section for the reaction $p + p \rightarrow \pi^+ + d$ in this form,[48] and give the $\ell = 0$ portion as

$$\sigma_s(p + p \rightarrow \pi^+ + d) = (0.138 \pm 0.015)\eta \text{ mb.} \qquad (29)$$

If Coulomb corrections are neglected, charge symmetry in strong interactions predicts

$$\sigma_s(n + n \rightarrow \pi^- + d) = \sigma_s(p + p \rightarrow \pi^+ + d) . \qquad (30)$$

Detail balance arguments give the reverse reaction cross section as

$$\sigma_s(\pi^- + d \rightarrow n + n) = \frac{2}{3} \frac{P_n^2}{P_\pi^2} \sigma_s(n + n \rightarrow \pi^- + d) , \qquad (31)$$

where the $2/3$ comes from the spin multiplicities of initial and final states, and P_n and P_π are the neutron and pion center-of-mass momentum. Here $P_\pi = m_\pi c \eta$, while p_n does not vary appreciably for small changes of η near $\eta = 0$ and can be treated as constant. According to this chain of reasoning the s-wave nonradiative cross section becomes

$$\sigma_s(\pi^- + d \rightarrow n + n) = (0.625 \pm 0.068)\eta^{-1} \text{ mb.} \qquad (31A)$$

The transition rate for a reaction going from state A to state B is given by the "Golden Rule" as

$$\omega_{AB} = \frac{2\pi}{\hbar} \left| H_{BA} \right|^2 \frac{dN_B}{dE} . \qquad (32)$$

For low-energy π^- in the reaction $\pi^- + d \rightarrow 2n$, the phase space, $\frac{dN_B}{dE}$, is determined only by the Q of the reaction and therefore is constant. In calculating the ratio of the pion transition rate for low

positive energies, ω_s, to the pion capture rate from the K shell, ω, only the interaction matrix H_{AB} need be considered. This ratio can then be written

$$\frac{\omega_s}{\omega} = \frac{\left| \int \phi_f^* (\vec{r})\, H_{int}\, \phi_s(\vec{r})\, d\tau \right|^2}{\left| \int \phi_f^* (\vec{r})\, H_{int}\, \phi_k(\vec{r})\, d\tau \right|^2} , \tag{33}$$

where $\phi_s(\vec{r})$ is the initial wave function, $\phi_k(\vec{r})$ is the K-shell meson wave function, $\phi_f(\vec{r})$ is the final-state wave function, and H_{int} is the interaction Hamiltonian. For interactions whose range is short compared with the wavelength of the initial state, Eq. (33) becomes

$$\frac{\omega_s}{\omega} = \frac{\left| \phi_s(\vec{r}) \right|^2}{\left| \phi_k(\vec{r}) \right|^2} = \frac{\left| \phi_s(0) \right|^2}{\left| \phi_k(0) \right|^2} . \tag{34}$$

The initial wave function can be written

$$\phi_s(\vec{r}) = e^{ikz} , \tag{35}$$

where k is the pion momentum and z the direction of incident beam. As the pion kinetic energy, T_{π^-}, approaches zero,

$$\lim_{T_{\pi^-} \to 0} \phi_s(\vec{r}) = \lim_{k \to 0} e^{ikz} = \frac{\sin kr}{kr} \approx 1. \tag{36}$$

Therefore $\left| \phi_s(0) \right|^2 = 1$.

The K-shell pion wave function can be written

$$\phi_k(r) = (\pi b_0^{\,3})^{-1/2}\, e^{-r/b_0} , \tag{37}$$

where b_0 is the Bohr radius. Then

$$\phi_k(0) = (\pi b_0^{\,3})^{-1/2} ,$$

or

$$\left| \phi_k(0) \right|^2 = (\pi b_0^{\,3})^{-1} .$$

The rate for low-energy transitions can be expressed as the incoming flux of particles, or the relative velocity, v, of the initial-state particle times the reaction cross section. Therefore

$$\frac{\omega_s}{\omega} = \frac{v\sigma_s}{\omega} = \pi b_0^3 \tag{38}$$

or

$$\omega = \frac{v}{\pi b_0^3}\ \sigma_s \ . \tag{39}$$

The relative velocity, v, can be related to the pion center-of-mass velocity β_π by

$$v = \beta_\pi \left(1 + \frac{m\pi}{M_{nuc}}\right) , \tag{40}$$

where m_π and M_{nuc} are the masses of the pion and nucleus respectively. Since, for small β, η can be written $\eta = \gamma\beta = \beta$, Eq. (39) can be written

$$\omega = \left(\frac{c}{\pi b_0^3}\right)\ \sigma_s\ \eta \left(1 + \frac{m_\pi}{M_{nuc}}\right) . \tag{41}$$

Using relation (31A) for σ_s gives the capture rate

$$\omega(\pi^- + d \rightarrow n + n) = (7.11 \pm 0.77) \times 10^{14}\ \text{sec}^{-1} . \tag{42}$$

The radiative-capture rate for pions in deuterium is related to the pion radiative-capture rate in hydrogen through the theoretical ratio T:

$$T = \frac{\omega(\pi^- + d \rightarrow n + n + \gamma)}{\omega(\pi^- + p \rightarrow n + \gamma)} \ . \tag{28}$$

Hamilton and Woolcock[12] found the pion photoproduction cross section in hydrogen near threshold to be of the form

$$\sigma_s(\gamma + p \rightarrow \pi^+ + n) = (0.197 \pm 0.015)\ \eta\ \text{mb.} \tag{43}$$

This result was achieved by fitting a dispersion relation to the existing data. They followed a similar procedure with data for the pion photoproduction on neutrons (obtained by applying the impulse approximation to pion photoproduction in deuterium) and arrived at a value of 1.33 for the ratio

$$r = \frac{\sigma_s(\gamma + n \rightarrow \pi^- + p)}{\sigma_s(\gamma + p \rightarrow \pi^+ + n)} \ . \tag{44}$$

A more recent value of r has been obtained by Swanson,[48] who applied the Coulomb corrections suggested by Baldin,[10] to his data for photopion production in deuterium. Swanson's value of r = 1.27±0.11, when coupled with Eq. (43), yields

$$\sigma_s(\gamma + n \rightarrow \pi^- + p) = (0.250 \pm 0.029)\,\eta \text{ mb.} \tag{45}$$

Upon application of the detailed balance argument the reverse-reaction cross section becomes

$$\sigma_s(\pi^- + p \rightarrow n + \gamma) = \left(\frac{P_\gamma}{P_{\pi^-}}\right)^2 \frac{G_\gamma}{G_{\pi^-}}\,\sigma_s(\gamma + n \rightarrow \pi^- + p)\,, \tag{46}$$

where $g_\gamma/g_{\pi^-} = 2$ are the spin multiplicities for the initial and final states, and $P_\pi = M_\pi c\,\eta$ and P_γ are the momenta of the pion and photon in the center-of-mass system. Near threshold P_γ can be treated as a constant. With the value for $\sigma_s(\gamma + n \rightarrow \pi^- + p)$ given in Eq. (45), Eq. (46) becomes

$$\sigma_s(\pi^- + p \rightarrow n + \gamma) = (0.43 \pm 0.05)\eta^{-1} \text{ mb.} \tag{47}$$

Using Eq. (41) the radiative-capture rate in hydrogen becomes

$$\omega(\pi^- + p \rightarrow n + \gamma) = (4.28 \pm 0.50) \times 10^{14} \text{ sec}^{-1}\,. \tag{48A}$$

The value for Eq. (45) obtained by Hamilton and Woolcock using the impulse approximation on pion photoproduction in deuterium yields, for the radiative-capture rate,

$$\omega(\pi^- + p \rightarrow n + \gamma) = (4.48 \pm 0.33) \times 10^{14} \text{ sec}^{-1}\,. \tag{48B}$$

Hamilton and Woolcock have reexamined the pion s-wave lengths and found they are best represented by values

$$a_1 - a_3 = 0.265 \pm 0.007\,. \tag{49}$$

The pion charge-exchange cross section can be related to the s-wave scattering lengths at low energies through charge independence. This relation is expressed by

$$\sigma_s(\pi^- + p \rightarrow \pi^0 + n) = \frac{8}{9}\,\pi \lambda_c^{\,2}(a_1 - a_3)^2(v^0/v^-)\,, \tag{50}$$

where the coefficient 8/9 is the appropriate Clebsch-Gordan coefficient, λ_c is the pion Compton wave length, a_1 and a_3 are the s-wave scattering lengths, and v^0/v^- is the ratio of the neutral pion velocity to the negative pion velocity. The term v^0/v^- appears due to the mass difference between charged and neutral pions. At very low energy v^0 can be taken as a constant. With the value of (49) used for the scattering length, Eq. (50) becomes

$$\sigma_s(\pi^- + p \rightarrow \pi^0 + n) = (0.796 \pm 0.029)\eta^{-1} \text{ mb.} \qquad (51A)$$

From Eq. (41) the charge-exchange capture rate is found to be

$$\omega(\pi^- + p \rightarrow \pi^0 + n) = (7.92 \pm 0.29) \times 10^{14} \text{ sec}^{-1} . \qquad (52)$$

The charge-exchange capture rate in hydrogen is related to the radiative-capture rate by the Panofsky ratio,

$$P = \frac{\omega(\pi^- + p \rightarrow \pi^0 + n)}{\omega(\pi^- + p \rightarrow \gamma + n)} . \qquad (53)$$

With use of the weighted value of the measurements of P given in Table II (i.e., $P = 1.534 \pm 0.018$) the radiative capture rate in hydrogen becomes

$$\omega(\pi^- + p \rightarrow n + \gamma) = (5.16 \pm 0.29) \times 10^{14} \text{ sec}^{-1}. \qquad (48C)$$

Miyake, Kinsey, and Knapp measured the pion charge-exchange cross section in hydrogen[43] and determined that their data were consistent with an s-wave cross section of the form

$$\sigma_s(\pi^- + p \rightarrow \pi^0 + n) = (0.839 \pm 0.109)\eta^{-1} \text{ mb.} \qquad (51B)$$

This value would lead to a radiative-capture rate of

$$\omega(\pi^- + p \rightarrow n + \gamma) = (5.44 \pm 0.71) \times 10^{14} \text{ sec}^{-1} . \qquad (48D)$$

The error-weighted average value of the independently calculated radiative-capture rates (48A), (48B), (48C), and (48D) is

$$\omega(\pi^- + p \rightarrow n + \gamma) = (4.93 \pm 0.16) \times 10^{14} \text{ sec}^{-1}. \qquad (48)$$

Traxler calculated T,[24] using the impulse approximation, and obtained 0.83±0.08. Using this value of T and the weighted average value of the calculated radiative-capture rate in hydrogen (48), one finds the radiative capture rate in deuterium to be

$$\omega(\pi^- + d \rightarrow n + n + \gamma) = (4.09\pm0.43)\times10^{14}\ \text{sec}^{-1}. \qquad (54)$$

Combining Eqs. (54) and (42) gives the deuterium ratio

$$S = 1.74\pm0.26. \qquad (55)$$

When Eq. (41) is rearranged, the expression for the s-wave cross section becomes

$$\sigma_s = \frac{\omega}{(C/\pi b_0^3)\,(1 + m_\pi/M_{nuc})}\ \eta^{-1}. \qquad (56)$$

when Eq. (56) is used the s-wave radiative absorption cross section at $T_\pi = 50$ MeV is

$$\sigma_s(\pi^- + d \rightarrow n + n + \gamma) = (0.43\pm0.05)\ \text{mb}. \qquad (57)$$

For 50-MeV incident pions Eq. (31A) predicts

$$\sigma_s(\pi^- + d \rightarrow n + n) = (0.747\pm0.081)\ \text{mb}. \qquad (58)$$

All values that were taken to be constant near $T_{\pi^-} = 0$ because they didn't vary strongly with T_{π^-} in that energy region were evaluated kinematically at $T_{\pi^-} = 0$.

All the calculated capture rates are summarized in Table X.

Table X. Capture rates calculated from s-wave pion relations

Reaction	Capture rate	Data used	Reference
$\omega(\pi^- + d \rightarrow n + n)$	$(7.11 \pm 0.77) \times 10^{14}$ sec^{-1}	$\sigma_s(pp \rightarrow \pi^+ d)$	28
$\omega(\pi^- + p \rightarrow \pi^0 + n)$	$(7.92 \pm 0.29) \times 10^{14}$ sec^{-1}	$\sigma_s(\pi^- p \rightarrow \pi^- p)$; $\sigma_s(\pi^+ p \rightarrow \pi^+ p)$	12
$\omega(\pi^- + p \rightarrow \pi^0 + n)$	$(8.35 \pm 1.09) \times 10^{14}$ sec^{-1}	$\sigma_s(\pi^- p \rightarrow \pi^0 n)$	30
$\omega(\pi^- + p \rightarrow n + \gamma)$	$(5.16 \pm 0.29) \times 10^{14}$ sec^{-1}	P; $\sigma_s(\pi^- p \rightarrow \pi^- p)$; $\sigma_s(\pi^+ p \rightarrow \pi^+ p)$	
$\omega(\pi^- + p \rightarrow n + \gamma)$	$(5.44 \pm 0.71) \times 10^{14}$ sec^{-1}	P; $\sigma_s(\pi^- p \rightarrow \pi^0 n)$	
$\omega(\pi^- + p \rightarrow n + \gamma)$	$(4.28 \pm 0.50) \times 10^{14}$ sec^{-1}	r; $\sigma_s(\gamma p \rightarrow \pi^+ n)$	29;12
$\omega(\pi^- + p \rightarrow n + \gamma)$	$(4.48 \pm 0.33) \times 10^{14}$ sec^{-1}	$\sigma_s(\gamma d \rightarrow \pi^- 2p)$ Impulse approx.	12
$\omega(\pi^- + p \rightarrow n + \gamma)$	$(4.93 \pm 0.16) \times 10^{14}$	Weighted average	
$\omega(\pi^- + d \rightarrow n + n + \gamma)$	$(4.09 \times 0.43) \times 10^{14}$ sec^{-1}	T; $\omega(\pi^- p \rightarrow n\gamma)$	

REFERENCES

1. D. W. Joseph, Nuovo Cimento 16, 997 (1960).
2. A. S. Wightman, Phys. Rev. 77, 521 (1950).
3. J. Fields, G. B. Yodh, M. Derrick, and J. G. Tetkovich, Phys. Rev. Letters 5, 69 (1960).
4. J. E. Russell and G. L. Shaw, Phys. Rev. Letters 4, 369 (1960).
5. T. B. Day, G. A. Snow, and J. Sucher, Phys. Rev. Letters 3, 61 (1959).
6. W. K. H. Panofsky, R. L. Aamodt, and J. Hadley, Phys. Rev. 81, 565, (1951).
7. W. Chinowsky and J. Steinberger, Phys. Rev. 100, 1476 (1955).
8. H. L. Anderson and E. Fermi, Phys. Rev. 86, 794 (1952).
9. K. A. Brueckner, R. Serber, and K. M. Watson, Phys. Rev. 81, 575 (1951).
10. A. Baldin, Nuovo Cimento 8, 569 (1958).
11. M. Cini, R. Gatto, E. L. Goldwasser, and M. Ruderman, Nuovo Cimento 10, 243 (1958).
12. J. Hamilton and W. S. Woolcock, Phys. Rev. 118, 291 (1960).
13. C. P. Sargent, R. Cornelius , M. Rinehart, L. M. Lederman and K. Rodgers, Phys. Rev. 109, 533 (1958).
14. J. M. Cassells, G. Fidecaro, A. Wetherell, and J. R. Wormald, Proc. Phys. Soc. (London) A70, 405 (1957).
15. J. Fischer, R. March, and L. Marshall, Phys. Rev. 109, 533 (1958).
16. J. Kuehner, A. W. Merrison, and S. Tornabene, Proc. Phys. Soc. (London)A73, 545 (1959).
17. L. Koller and A. M. Sachs, Phys. Rev. 116, 760 (1959).
18. A. F. Dunaitsev, V. S. Panteuv, Yu. D. Prokoshkin, Fang Syoa-Wei, and M. N. Khachaturyan in Proceedings of the 1960 Annual International Conference on High-Energy Physics, Rochester, edited by E. C. G. Sudarshan, J. H. Tinlot, and A. C. Melissions (Interscience Publishers, Inc., New York, 1960), p. 181.
19. M. Derrick, J. Tetkovich, T. Fields and J. Deahl, Phys. Rev. 120, 1022 (1960).

20. N. P. Samios, Phys. Rev. Letters 4, 470 (1960).

21. D. P. Jones, P. G. Murphy, P. L. O'Neill, and J. R. Wormald, Proc. Phys. Soc. (London) A77, 77 (1961).

22. V. T. Cocconi, T. Tazzini, G. Fidecaro, M. Legros, N. H. Lipman, and A. W. Merrison, Nuovo Cimento 22, 494 (1961).

23. J. W. Ryan, Phys. Rev. 130, 1554 (1963).

24. Robert H. Traxler, Two Topics in Pion Physics, I. Photoproduction of Neutral Pions from Complex Nuclei and the Pair-Correlation Function, and II. The Relative Rate of Absorption of Negative Pions in Hydrogen and Deuterium (Thesis), Lawrence Radiation Report UCRL-10417, Aug. 1962 (unpublished).

25. W. Chinowsky and J. Steinberger, Phys. Rev. 95, 1561 (1954).

26. J. A. Kuehner, A. W. Merrison, and S. Tornabene, Proc. Phys. Soc. (London) A73, 551 (1958).

27. W. C. Bowman, J. B. Carroll, and J. A. Poirier, Rev. Sci. Instr. 33, 741 (1962).

28. Thomas J. Devlin, Jr., Lawrence Radiation Laboratory Report UCRL-9727, Sept. 1961, (unpublished).

29. Howard S. Goldberg, Joesph D. Good, and Morris Pripstein (Lawrence Radiation Laboratory), private communication.

30. A. E. Bjerke, Q. A. Kerns, and T. A. Nunamaker, IRE Trans. Nucl. Sci. NS-9, 314 (1962).

31. Dudley B. Chelton and Douglas B. Mann, Lawrence Radiation Laboratory Report UCRL-3421, May 1956 (unpublished).

32. A. Kantz and R. Hofstadter, Nucleonics 12, 3, 36 (1954).

33. G. L. Schnurmacher, Rev. Sci. Instr. 32, 1380 (1961).

34. Richard J. Kurz, Differential Distributions of Neutrons in Inelastic π^-p Interactions at 374, 417, and 454 MeV (Thesis), Lawrence Radiation Laboratory Report UCRL-10564, Nov. 1962 (unpublished).

35. R. H. Moore and R. K. Zeigler, The Solution of the General Least-Squares Problem with Special Reference to High-Speed Computers, Los Alamos Scientific Laboratory Report LA-2367, Oct. 1959 (unpublished).

36. Jim B. Carroll (Lawrence Radiation Laboratory), private communication.
37. L. Champomier and J. Hanna, Lawrence Radiation Laboratory, Alvarez Memo No. 389 (unpublished).
38. Robert Belsche (Lawrence Radiation Laboratory), private communication.
39. R. T. Birge, Rev. Mod. Phys. 13, 233 (1941).
40. R. Durbin, H. Loar, and J. Steinberger, Phys. Rev. 84, 581 (1951).
41. A. Roberts and J. Tinlot, Phys. Rev. 90, 951 (1953).
42. W. Spry, Phys. Rev. 95, 1295 (1954).
43. K. Miyake, K. F. Kinsey, and D. E. Knapp, Phys. Rev. 126, 2188 (1962).
44. J. Tinlot and A. Roberts, Phys. Rev. 95, 137 (1954).
45. G. M. York, W. J. Kernan, and E. L. Garwin, Phys. Rev. 119, 1096 (1960).
46. D. Bodansky, A. M. Sachs, and J. Steinberger, Phys. Rev. 93, 1367 (1954).
47. D. N. Edwards, S. G. F. Frank, and J. R. Holt, Proc. Phys. Soc. (London), A73, 856 (1959).
48. F. S. Crawford, Jr., and M. L. Stevenson, Phys. Rev. 97, 1305 (1955).
49. William P. Swanson, Photopion Production from Deuterium Near Threshold (Thesis), Lawrence Radiation Laboratory Report UCRL-9194, April 1960 (unpublished).